Title

Assembly of neuron- and radial glial cell-derived extracellular matrix molecules promotes radial migration of developing cortical neurons

Author names

Ayumu Mubuchi[1], Mina Takechi[2], Shunsuke Nishio[3], Tsukasa Matsuda[3], Chihiro Sato2[2,4,5], Ken Kitajima[2,4,5], Hiroshi Kitagawa[6], Shinji Miyata[1,*]

Affiliations

[1]Graduate School of Agriculture, Tokyo University of Agriculture and Technology, 3-5-8 Saiwaicho, Fuchu, Tokyo, 183-8509, Japan

[2]Graduate School of Bioagricultural Sciences, Nagoya University, Furocho, Chikusa-Ku, Nagoya, 464-8601, Japan

[3]Faculty of Food and Agricultural Sciences, Fukushima University, Kanayagawa 1, Fukushima, 960-1296, Japan

[4]Bioscience and Biotechnology Center, Nagoya University, Furocho, Chikusa-Ku, Nagoya, 464-8601, Japan

[5]Institute for Glyco-core Research, Nagoya University, Furocho, Chikusa-Ku, Nagoya, 464-8601, Japan

[6]Laboratory of Biochemistry, Kobe Pharmaceutical University, 4-19-1 Motoyamakitamachi, Higashinada-Ku, Kobe, 658-8558, Japan

*Correspondence: smiyata@go.tuat.ac.jp

Abstract

Radial neuronal migration is a key neurodevelopmental event for proper cortical laminar organization. Newly born neurons migrate in a complex three-dimensional environment generated by the extracellular matrix (ECM), secreted factors, and neighboring cells. However, the molecular mechanisms by which the ECM controls radial migration remain largely unknown. We herein identified neurocan (NCAN), a risk factor for neuropsychiatric disorders, as a major chondroitin sulfate proteoglycan produced by developing cortical neurons. NCAN binds to both radial glial cell-derived tenascin-C (TNC) and hyaluronan (HA), a large linear polysaccharide, forming a ternary complex of NCAN, TNC, and HA. Developing cortical neurons make contact with the ternary complex during migration. The enzymatic or genetic disruption of the ternary complex impairs radial migration by suppressing the multipolar-to-bipolar transition. Furthermore, TNC in the ternary complex promotes neuronal morphological maturation. The present results provide evidence for the cooperative role of neuron- and radial glial cell-derived ECM molecules in cortical development.

Keywords

Extracellular matrix; Cortical development; Radial migration; Proteoglycans; Hyaluronan; Tenascin

Introduction

The six-layered laminar structure of the mammalian cerebral cortex is achieved via the coordinated radial migration of neurons from their place of birth in the ventricular zone (VZ) to their final destination in the cortical plate (CP) [1–3]. Radial glial cells residing in the VZ are embryonic neural stem cells and a major source of neurons [4]. During the neurogenesis period (from embryonic day (E) 12 to E18 in mice), radial glial cells divide asymmetrically to give rise to one self-renewing radial glial cell and one intermediate progenitor cell. Intermediate progenitor cells detach from the apical surface, lose their polarity, and further divide symmetrically to produce a pair of neurons above the VZ [5]. Newly born immature neurons transiently become multipolar shapes with multiple neurites and move in random directions [5,6]. Neurons then change their shape from multipolar to bipolar, extending leading and trailing processes in the subplate/intermediate zone (SP/IZ) [7–10]. Bipolar neurons attach to the radial fibers elongated from radial glial cells and migrate radially along these fibers towards their final destination in the CP [11]. Therefore, radial glial cells play important dual roles in the production of neurons and guiding them to their proper location.

The leading and trailing processes of bipolar neurons eventually become the apical dendrite and axon. Therefore, the multipolar-to-bipolar transition is a critical step in establishing neuronal polarity. The intrinsic mechanisms underlying neuronal polarity have been investigated for a long time using primary cultured neurons *in vitro* and the importance of cytoskeletal molecules, signaling cascades, and transcription factors has been demonstrated [12–14]. Polarity formation *in vivo* may differ from that *in vitro* because it occurs in a complex three-dimensional environment generated by the extracellular matrix (ECM), secreted factors, and neighboring cells. Notably, the multipolar-to-bipolar transition occurs in the SP/IZ, a cell-sparse area rich in ECM molecules [15–20]. However, the function of the embryonic ECM, particularly in radial migration, has only been partly elucidated [21].

The ECM provides structural support to guarantee tissue integrity and regulates neuronal differentiation, maturation, and synaptic function in the brain. The brain ECM is characterized by a predominance of chondroitin sulfate proteoglycans (CSPGs) [22–25]. In contrast to other tissues in the body, fibronectin and collagen are not abundant in the brain ECM. CSPGs expressed in the brain, including neurocan (NCAN), aggrecan (ACAN), versican, and brevican, share structural domains [26,27]. The N-terminal domain interacts with hyaluronan (HA), a large linear polysaccharide chain that reaches several million Da in size. The central region shows an extended structure and contains covalently bound chondroitin sulfate chains. The C-terminal domain binds to tenascins, a group of multimeric glycoproteins. Therefore, CSPGs, HA, and tenascins form a macromolecular complex in the extracellular space.

We previously reported that HA accumulated in the SP/IZ of the developing mouse cerebral cortex [28]. We herein demonstrated that NCAN, a major CSPG produced by developing cortical neurons, bound to HA in the SP/IZ *in vivo*. NCAN also interacted with radial glial cell-derived tenascin-C (TNC), forming a ternary complex of HA, NCAN, and TNC. Developing cortical neurons made contact with the ternary complex during migration. The enzymatic or genetic disruption of the ternary complex retarded radial migration by suppressing the multipolar-to-bipolar transition. TNC was identified as an active component in

the ternary complex that promoted neuronal morphological maturation. The present results provide evidence for the cooperative role of neuron- and radial glial cell-derived ECM molecules in cortical development.

Results

NCAN is a major CSPG produced by developing cortical neurons.

We attempted to identify the core proteins of CSPGs in the developing mouse brain using an antibody recognizing the neoepitope generated at the non-reducing terminus of chondroitin sulfate chains after digestion with chondroitinase ABC (Fig. 1A) [29,30]. An immunoblot analysis of the mouse cerebral cortex at E18 indicated that a band at 130 kDa represented a major CSPG detected by the anti-neo epitope antibody (Fig. 1B). However, the developing mouse cerebral cortex contained other minor CSPGs. The lack of staining from the undigested cerebral cortex confirmed the specificity of the antibody. In-gel tryptic digestion followed by a MALDI-TOF/TOF analysis identified the 130-kDa CSPG as an N-terminal portion NCAN (Fig. 1C). Full-length >250-kDa NCAN is reportedly cleaved to generate the N-terminal 130-kDa fragment and C-terminal 150-kDa fragment (Fig. 1D) [31]. Using an antibody to the N-terminal portion of NCAN, we found that the full-length and cleaved fragment of NCAN were both detected in the developing cerebral cortex. In contrast, only the cleaved fragment was identified in the adult cerebral cortex, indicating the developmental stage-dependent proteolytic processing of NCAN (Fig. 1E, F).

A quantitative PCR analysis showed high expression levels of NCAN during the late embryonic and early postnatal stages (Fig. 1G). Using the *in utero* electroporation-mediated labeling of progenitor cells in the VZ with GFP at E14 and subsequently isolating GFP-positive cells from the cerebral cortex, we found that NCAN expression increased two days after labeling and was thereafter maintained (Fig. 1H). Primary cultured cortical neurons gradually secreted the full-length and N-terminal fragment of NCAN into the culture medium (Fig. 1I). These results supported cortical neurons being the primary source of NCAN during development.

Neuron-derived NCAN forms a pericellular matrix with HA.

Immunostaining of the developing cerebral cortex showed that NCAN densely accumulated in cell-sparse zones, such as the MZ and SP/IZ, but was less abundant in cell-dense regions, such as the CP and VZ (Fig. 2A). In contrast, *in situ* hybridization revealed the wide distribution of *Ncan* mRNA throughout the cerebral cortex (Fig. 2B), implying a mechanism for localizing the secreted NCAN protein in the SP/IZ and MZ. The localization pattern of the NCAN protein was similar to that of HA, which we previously reported (Fig. 2C) [28]. Furthermore, NCAN and HA co-localized in cortical neuronal cultures as punctate signals at adhesion sites between the neuron and culture substrate, indicating that NCAN formed a pericellular matrix with HA (Fig. 2D).

To directly examine binding between NCAN and HA, we pulled down endogenous HA and its interacting proteins using a biotinylated HA-binding protein (b-HABP), followed by immunoblotting with the antibody to the N-terminal portion of NCAN (Fig. 2E). This analysis confirmed the interaction between

NCAN and endogenous HA (Fig. 2F). NCAN did not precipitate without b-HABP. The precipitation of NCAN depended on intact HA because NCAN disappeared from precipitates by digestion with hyaluronidase from *Streptomyces hyalurolyticus*, which specifically degrades HA and does not act on other glycosaminoglycans [32]. In addition, exogenously added biotinylated HA (b-HA) also bound to the N-terminal portion of NCAN (Fig. 2G).

Radial glial cell-derived TNC interacts with the C-terminal portion of NCAN.

To further screen the interacting partners of NCAN, we pulled down proteins in the embryonic mouse brain lysate with GFP fused-NCAN immobilized to resin (Fig. 3A). Tryptic digestion followed by a LC-MS/MS analysis identified TNC as a major interactor for NCAN (Fig. 3B, C). The expression of TNC at mRNA and protein levels peaked during late embryonic brain development, similar to the expression pattern of NCAN (Fig. 3D-F). The mRNA expression of TNC only in the VZ at E16 indicated that radial glial cells produced TNC, as previously proposed (Fig. 3G) [33]. However, the TNC protein was not restricted to the VZ, it was also found in the SP/IZ and MZ (Fig. 3H).

Pull-down experiments showed that the C-terminal half, but not the N-terminal half of NCAN bound to TNC (Fig. 4A, B), which is consistent with previous findings [34,35]. Interactions between NCAN and TNC were dependent on a divalent cation, but not on chondroitin sulfate chains on NCAN (Fig. 4B). We performed AlphaFold2 multimer and predicted a complex structure of NCAN and TNC (Fig. 4C, Supplemental Fig. 1). In this modeled complex, a C-type lectin domain (CLD) of NCAN interacts with the 4th and 5th fibronectin type-III domains (FNIII) of TNC, which is consistent with a previously reported structure of aggrecan (ACAN) and tenascin-R (TNR) (Supplemental Fig. 1)[36]. Amino acid residues in the interface of NCAN-TNC and ACAN-TNR complex were highly conserved (Fig. 4D, E). An Asn residue (Asn1148 in mNCAN and Asn2022 in rACAN), which interacts with Ca^{2+} ions, was also conserved (Fig. 4D, E). Sequence alignments of fourteen FNIII of TNC indicated that the amino acid residues in FNIII-4 involved in the binding to NCAN are not well conserved among other FNIII (Supplemental Fig. 1).

HA, NCAN, and TNC from the ternary complex in the developing cerebral cortex.

We found that HA, NCAN, and TNC co-localized in the upper part of the SP/IZ and MZ of the embryonic mouse cerebral cortex at E17 (Fig. 5A). High magnification views showed the aggregate-like deposition of these molecules in the SP/IZ, suggesting the formation of a ternary complex. To clarify the formation of the ternary complex *in vivo*, we degraded HA at E14 by an intraventricular injection of hyaluronidase from *S. hyalurolyticus*. Most HA disappeared from the cerebral cortex two days after the injection (Fig. 5B). We noted that the staining intensity of NCAN and TNC decreased at the SP/IZ following the hyaluronidase treatment, indicating the interaction of these molecules and the requirement of HA for the localization of NCAN and TNC. An immunoblot analysis showed that the digestion of HA significantly reduced the amount of NCAN and TNC in the cerebral cortex, confirming the essential role of HA in the retention of NCAN and TNC (Fig. 5C).

To examine whether NCAN and TNC are required for the localization of HA in the cerebral cortex, we generated double knockout (DKO) mice for NCAN and TNC (Supplemental Fig. 2). Although the total amount of HA did not significantly differ between wild-type (WT) and DKO brains (Supplemental Fig. 2), HA in DKO mice was more diffusely distributed than that in WT mice (Fig. 5D). These results indicated that NCAN and TNC were necessary for HA to accumulate in the SP/IZ and *vice versa*. We proposed that NCAN, HA, and TNC cooperatively assemble a supramolecular complex as follows: (1) NCAN derived from developing neurons binds to multiple sites on a long chain of HA via the N-terminal Link modules; (2) The hexamer of TNC secreted from radial glial cells cross-links NCAN by binding to their C-terminal CLD domains (Fig. 5E).

Disruption of the ternary complex retarded neuronal migration.

To investigate whether the ternary complex interacts with the neuronal surface *in vivo*, we labeled developing cortical neurons with a membrane-bound form of GFP by transfecting the plasmids into radial glial cells residing in the VZ on E14 (Fig. 6A). Three days after *in utero* electroporation, GFP-positive neurons exhibited a bipolar morphology in the upper SP/IZ and CP, as previously reported (Fig. 6B, C) [6]. Z-stack projections of confocal images revealed that the ternary complex frequently contacted the surface of migrating neurons (Fig. 6B, C). Orthogonal views of 3D images clearly showed the extracellular deposition of the ternary complex surrounding the cell body and neurites of bipolar neurons (Fig. 6B, C)

These results prompted us to examine the role of the ternary complex in neuronal migration. Since the migratory patterns of neurons differ between the lateral and medial cortices, we took advantage of Flash Tag technology, in which an intraventricular injection of fluorescent dyes allows for the pulse labeling of progenitors in contact with the ventricle across the brain [37–39]. Radial glial cells in the M-phase were labeled at E14, and their progeny was analyzed two days later at E16. In the lateral cortex of WT mice, many labeled cells were migrating in the upper and lower SP/IZ, and a smaller population had already reached the CP (Fig. 6D, E). In DKO mice, most cells resided beneath the lower SP/IZ, and very few reached the upper SP/IZ and CP. In the medial cortex of WT mice, neurons reached the CP more quickly than in the lateral cortex (Fig. 6D, F) [39]. DKO mice exhibited slower neuronal migration in the medial cortex than WT mice, suggesting that the ternary complex facilitated the entry of neurons into the CP in a wide range of cortical regions. Delayed migration in DKO mice was restored after three days of labeling, suggesting that the ternary complex was only transiently required for neuronal migration (Supplemental Fig. 3).

We investigated whether the deletion of NCAN and TNC affected radial glial cells in the VZ. The number of Pax6-positive radial glial cells and Tbr2-positive intermediate progenitor cells and the morphology of nestin-positive radial fibers were indistinguishable between WT and DKO mice (Supplemental Fig. 4). These results suggested that the delay in neuronal migration was not due to the decreased proliferation of radial glial cells in DKO mice. We also examined the importance of the ternary complex by transiently depleting HA from WT mice. In comparisons with PBS-injected controls, a hyaluronidase injection at E14 significantly inhibited neuronal migration into the CP (Fig. 6G, H). The digestion of HA did not further affect

neuronal migration in the DKO background, indicating that HA, NCAN, and TNC acted in the same pathway (Supplemental Fig. 5).

DKO mice show delayed multipolar-to-bipolar transition during radial migration.

To gain insights into the mechanisms underlying migration defects, we investigated whether the loss of the ternary complex influenced the multipolar-to-bipolar transition. Fifty-three hours after *in utero* electroporation with a cytosolic form of mCherry, we evaluated neuronal morphology based on the following criteria: (1) the ratio of the length-to-width of labeled neurons as an indicator of cell shape; (2) the angle between major neurites and the ventricle surface; (3) the percentage of neurons with a bipolar morphology, defined as cells with a length-to-width ratio greater than three and an orientation angle greater than 70° (Fig. 7A). *In utero* electroporation-mediated labeling also showed delayed neuronal migration in DKO mice, similar to Flask Tag labeling (Fig. 7B). A morphological analysis revealed a significantly lower length-to-width ratio of neurons in DKO mice than in WT mice (Fig. 7C, D). This result indicated that control neurons had an elongated shape, whereas neurons in DKO mice retained a rounded shape. Many neurons radially extended their major neurites towards the pia surface (between 70° and 90° relative to the ventricle surface) in WT mice, which is characteristic of bipolar neurons (Fig. 7E). In comparisons with control neurons, the major neurites of DKO neurons were not directed towards the pia surface. Consistent with these results, we observed a significantly smaller proportion of bipolar neurons in DKO mice than in WT mice (Fig. 7F). Therefore, retarded neuronal migration in DKO mice was associated with defects in the multipolar-to-bipolar transition.

TNC promotes the neurite outgrowth and morphological maturation of cortical neurons.

The loss of one component of the ternary complex affects the localization of other components, making it challenging to identify the components responsible for the multipolar-to-bipolar transition *in vivo*. Therefore, we labeled progenitor cells with GFP at E14 by *in utero* electroporation and cultured dissociated neurons prepared at E15 on a glass plate coated with HA, NCAN, or TNC (Fig. 8A). This method allows us to analyze the effects of each component on morphological changes in cortical neurons at the same developmental stage *in vitro*. GFP-positive neurons on the control substrate, poly-L-ornithine (PLO), exhibited a typical morphological transition from stages 1 to 3 as follows (Fig. 8B, C): Neurons initially have immature processes (stage 1) and then begin to extend multiple neurites of approximately equal lengths (stage 2); One of the neurites rapidly elongates to become the axon (stage 3), corresponding to the multipolar-to-bipolar transition *in vivo*. Culturing neurons on TNC markedly accelerated the transition from stages 1 to 3 in a dose-dependent manner (Fig. 8C, D). After three days, 80% of the neurons cultured on TNC showed the stage 3 morphology, in contrast to only 40% of neurons on a control substrate. Closer observations revealed that TNC promoted neuritogenesis (as indicated by the increased number and total length of neurites) and axon elongation (as indicated by the increased length of the longest neurite) (Fig. 8E-G). In contrast to TNC, neither HA nor NCAN affected neuronal morphology (Fig. 8C-G, Supplemental Fig. 6), suggesting that TNC

was an active component in the ternary complex that stimulated the multipolar-to-bipolar transition during radial neuronal migration.

Discussion

The multipolar-to-bipolar transition of developing cortical neurons is essential for radial migration and neuronal polarity. Defects in the multipolar-to-bipolar transition lead to the neuronal mispositioning and disorganization of the laminar structure, resulting in the malformation of cortical development [40,41]. Therefore, the timing and location of the multipolar-to-bipolar transition needs to be tightly controlled. The present results propose that the assembly of ECM molecules in the SP/IZ provides an extracellular positional cue for migrating neurons that specify the site of the multipolar-to-bipolar transition.

Polarity formation *in vivo* occurs in a microenvironment or niche created in the SP/IZ. A previous study found that pre-existing efferent axon tracts in the SP/IZ interacted with migrating multipolar neurons to promote the formation of axons [7]. Secreted soluble factors also play significant roles in this process. A gradient of semaphorin 3A in the developing cerebral cortex regulates neuronal migration and polarity by attracting apical dendrites and repulsing axons [42,43]. Transforming growth factor-β initiates signaling pathways that specify axons [44]. Reelin, a glycoprotein secreted by Cajal-Retzius cells in the MZ, is essential for completing neuronal migration and cortical lamination [8,45]. Therefore, a combination of ECM molecules, secreted factors, and neighboring cells regulates neuronal polarity during cortical development.

Radial glial cells play a dual function during development: producing neurons and serving as scaffolds for neuronal migration. The present study discovered another role for radial glial cells: they secrete and deposit TNC to stimulate the morphological transition of migrating neurons in the SP/IZ. The source of TNC shifts from radial glial cells during neurogenesis to astrocytes during gliogenesis (E18 or later) in mice [33]. In gyrencephalic species, such as humans, basal/outer radial glial cells residing in the outer sub-VZ generate the majority of cortical neurons and are responsible for the expansion of the cerebral cortex [3,4]. Basal/outer radial glial cells are characterized by the high gene expression of several ECM molecules, including TNC [46,47], indicating that basal/outer radial glial cells create a microenvironment that promotes neuronal migration. In addition, HA-based ECM affects the cortical folding of the developing human neocortex [48], suggesting that the evolutionarily conserved ECM structure contributes to neocortex expansion in gyrencephalic species.

The tenascin gene family in vertebrates comprises four closely related members. They share structural motifs: a cysteine-rich region at the N terminus followed by EGF-like repeats, FNIIIs, and a fibrinogen-like globe at the C terminus. TNC monomers assemble to hexamers at the N-terminal region. Distinct domains of TNC are involved in cell adhesion, cell repulsion, and neurite outgrowth promotion [33,49–51]. For example, alternatively spliced FNIIIs stimulate neurite outgrowth by binding to neuronal surface contactin-1 in primary cultured neurons[52]. Several integrins have been identified as receptors for TNC, and through this interaction, TNC influences cell adhesion, migration, and proliferation [51]. However, the

mechanisms by which TNC secreted from radial glial cells is presented to neurons *in vivo* remain unclear. Our analysis revealed that binding to HA via NCAN was required for the deposition of TNC in the SP/IZ. Further studies are needed to identify receptors for TNC on migrating neurons and its downstream signaling pathway that transmits information from the extracellular environment to the inside of the cell.

There is a transition from embryonic- to adult-type ECM during brain development [23]. The expression of NCAN and TNC is high in the embryonic brain, whereas ACAN, brevican, and TNR increase during late postnatal development. In the adult brain, ACAN cross-links HA and TNR and forms macromolecular aggregates around subpopulations of neurons [53]. This condensed ECM structure, called perineuronal nets, is formed at the late postnatal stages and plays pivotal roles in neural plasticity, memory consolidation, and circuit maturation [54–57]. The ternary complex of ACAN, HA, and TNR physically stabilizes existing synapses and inhibits new synapse formation. The present study showed that a structurally similar ternary complex of NCAN, HA, and TNC was formed in the SP/IZ of the embryonic cortex, but exerted distinct functions in cortical development. Although the interaction of NCAN with HA and TNC was previously reported *in vitro*, the present results revealed for the first time the formation of the ternary complex *in vivo*. Full-length NCAN is detected during early development, but not in adulthood, indicating that the proteolytic cleavage of NCAN affects the assembly of the ternary complex. Screening using peptide library mixtures revealed that matrix metalloprotease-2 cleaved the central region of NCAN *in vitro* [58]. The temporal control of matrix metalloproteases may affect neuronal migration via the assembly and disassembly of the ECM.

NCAN is reportedly dispensable for brain development because NCAN-deficient mice have no apparent deficits in brain anatomy, morphology, or ultrastructure [59]. However, recent genome-wide association studies identified a genetic variation in NCAN as a risk factor for two neuropsychiatric disorders, bipolar disorder and schizophrenia [60,61]. The NCAN risk allele influences cortical folding and cognitive performance in healthy subjects [61,62]. Cerebral organoids from patients with bipolar disorder indicate the marked down-regulation of NCAN [63]. Although the underlying molecular mechanisms remain unknown, the present results suggest that impaired neuronal migration during development in the absence of NCAN contributes to the pathogenesis of neuropsychiatric disorders.

In conclusion, the present study revealed that the assembly of NCAN, HA, and TNC forms the microenvironment in the SP/IZ, in which the multipolar-to-bipolar transition occurs. We found that TNC in the ternary complex promoted the morphological transition of neurons, shedding light on radial glial cell-derived ECM in neuronal migration during development.

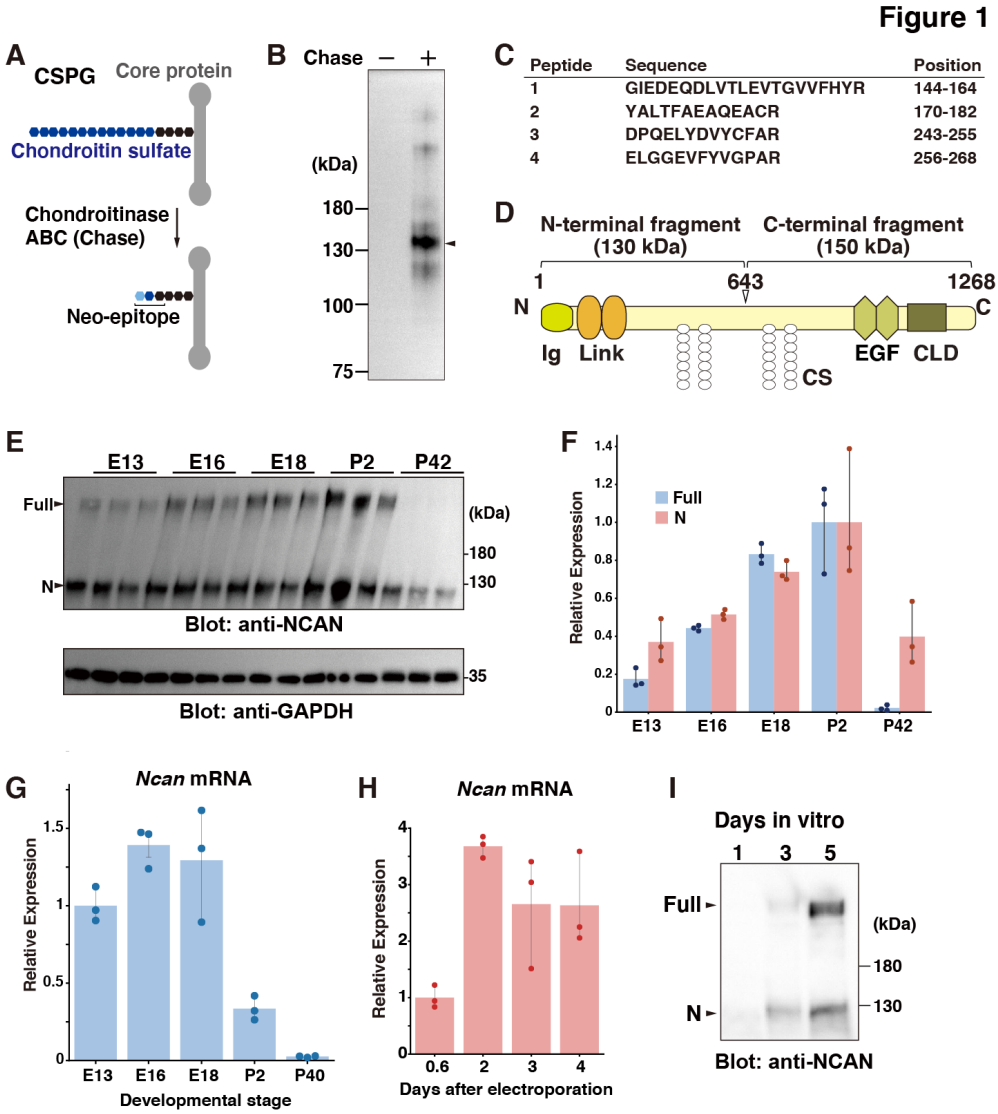

Fig. 1. NCAN is a major CSPG produced by developing cortical neurons.

(**A**) Detection of the neoepitope of CSPGs after digestion with chondroitinase ABC (Chase). (**B**) Immunoblotting of the neoepitope from undigested (Chase -) and digested (Chase +) cerebral cortex lysates prepared at E18. The arrowhead indicates the major CSPG at 130 kDa. (**C**) List of peptide fragments identified from the 130-kDa band. Positions indicate the amino acid number in full-length NCAN. (**D**) Domain structure of mouse NCAN. Ig: immunoglobulin-like domain, Link: hyaluronan-binding link module, EGF: epidermal growth factor-like repeat, CLD: C-type lectin domain, CS: chondroitin sulfate chain. (**E, F**) Developmental changes in NCAN expression from E13 to postnatal day (P) 42. The arrowheads indicate the full-length and N-terminal fragment of NCAN (E). Relative levels of the full-length (Full) and N-terminal fragment (N) of NCNA (F). Values are normalized to GAPDH and represented relative to P2. n = 3 for each point. Mean ± SD. (**G**) Expression levels of *Ncan* mRNA. Values are normalized to *Gapdh* and represented relative to E13. n = 3 for each point. Mean ± SD. (**H**) Expression of *Ncan* mRNA in GFP-labeled cells isolated on the indicated days after *in utero* electroporation. Values are normalized to *Gapdh* and represented relative to 0.6 days. n = 3 for each point. Mean ± SD. (**I**) Immunoblot analysis of NCAN in the cultured medium of primary cultured cortical neurons 1, 3, and 5 days after plating.

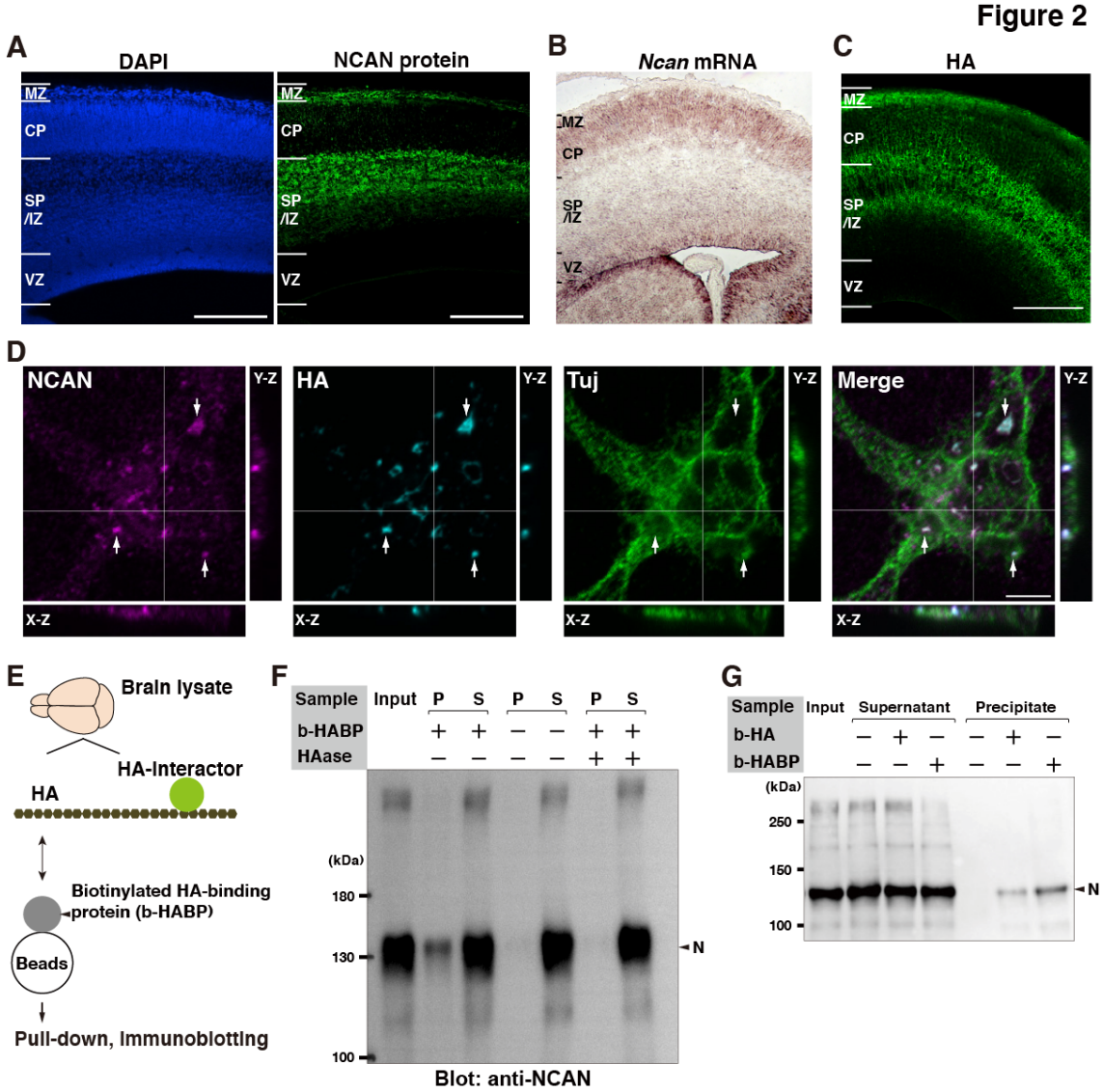

Fig. 2. Neuron-derived NCAN forms a pericellular matrix with HA.

(**A**) Localization of NCAN (green) in the E16 cerebral cortex. Nuclei were counterstained with DAPI (blue). (**B**) *In situ* hybridization analysis of *Ncan* mRNA on the E16 cerebral cortex. (**C**) Distribution of HA (green) visualized by the biotinylated HA-binding protein (b-HABP) in the E16 cerebral cortex. (**D**) High magnification views of a Tuj-positive primary cultured cortical neuron (green) 5 days after plating. White arrows indicate the co-localization of NCAN (magenta) and HA (cyan). Orthogonal projections in the X-Z and Y-Z planes taken along the white lines showed the localization of NCAN and HA at the adhesion sites between the neuron and culture substrate. (**E**) Schema of the pull-down assay for analyzing binding between endogenous HA and its interactors. (**F**) Immunoblotting of the input, precipitate (P), and supernatant (S) with an anti-NCAN antibody. NCAN was precipitated with HA by adding b-HABP (b-HABP +). NCAN was not precipitated without b-HABP (b-HABP -) or after digestion with hyaluronidase (HAase +). (**G**) Co-precipitation of NCAN with exogenously added biotinylated HA (b-HA +) or endogenous HA (b-HABP +). Scale bars represent 200 μm (A, C) and 5 μm (D).

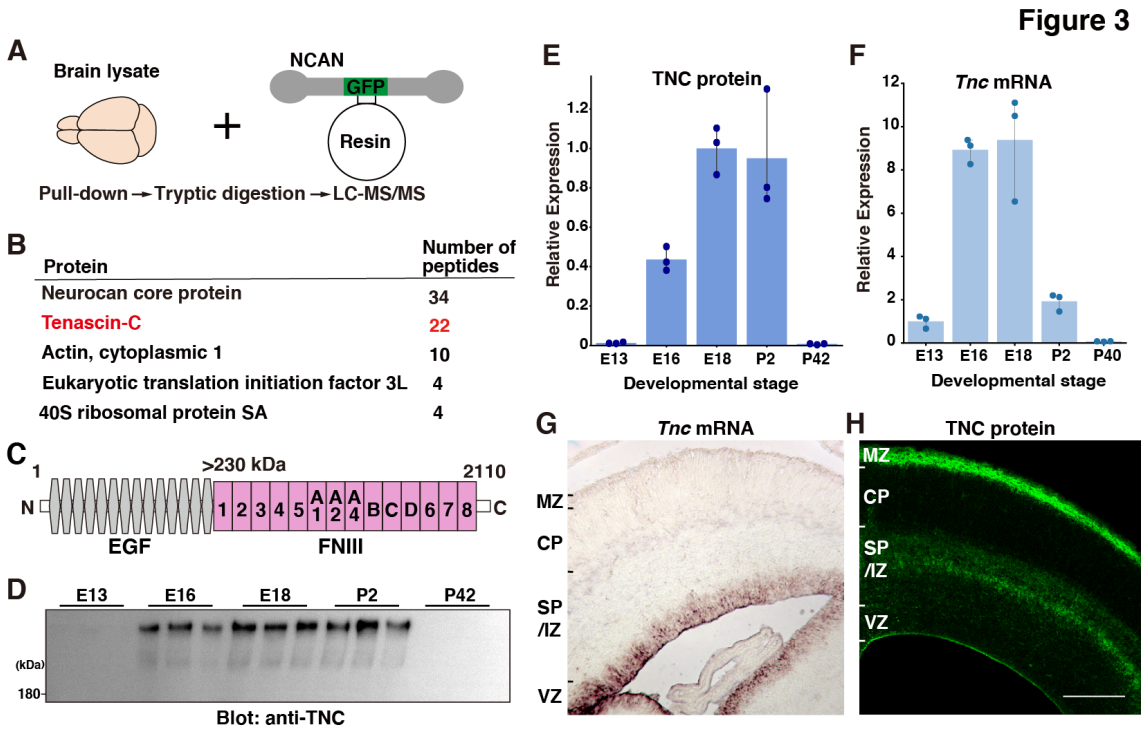

Fig. 3. Screening of the interacting partners of NCAN.

(**A**) Schematic of the pull-down assay to identify NCAN-interacting partners. (**B**) List of the top 5 proteins identified by a LC-MS/MS analysis. (**C**) Domain structure of mouse TNC. EGF: epidermal growth factor-like repeat, FNIII: fibronectin type-III domain. (**D**) Detection of TNC in cerebral cortex lysates prepared from E13 to P42. (**E, F**) Expression of the TNC protein (E) and *Tnc* mRNA (F) during cortical development. Values are normalized to GAPDH and represented relative to E18 (E) or E13 (F). n = 3 for each point. Mean ± SD. (**G, H**) Localization of *Tnc* mRNA (G) and the TNC protein (H) in the E16 cerebral cortex. Scale bars represent 200 µm.

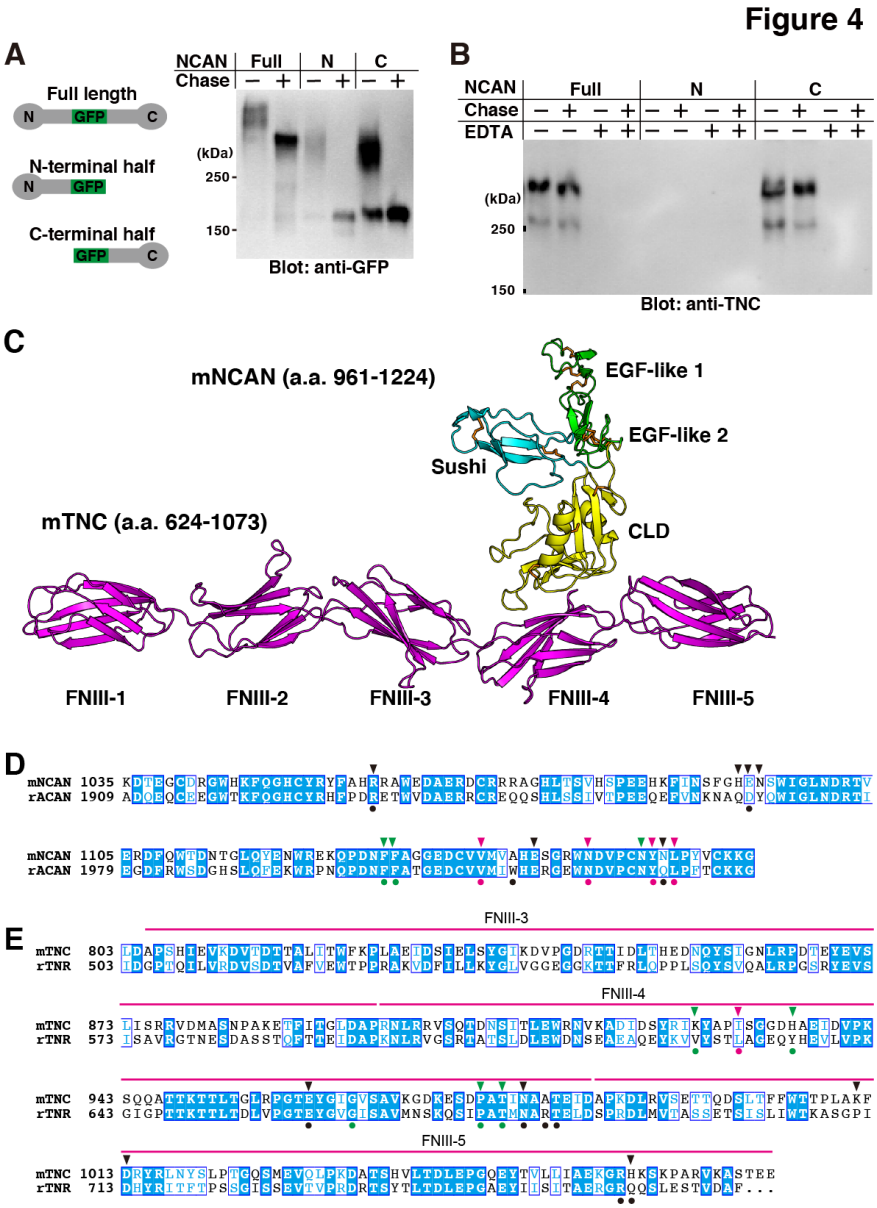

Fig. 4. Radial glial cell-derived TNC interacts with the C-terminal half of NCAN.

(**A**) Recombinant expression of the GFP-fused full-length, N-terminal half, and C-terminal half of NCAN. The culture medium of transfected HEK293 cells was digested with chondroitinase ABC (Chase) and analyzed by immunoblotting with an anti-GFP antibody. (**B**) Co-precipitation of TNC with the full-length and C-terminal half of NCAN. Interactions between NCAN and TNC disappeared following the addition of EDTA, but were not affected by Chase digestion. The N-terminal half of NCAN did not bind to TNC. (**C**) Alphafold2 prediction of mouse (m) NCAN-TNC complex. Five predicted complex models were generated using AlphaFold2 multimer implemented in ColabFold, and the best-predicted complex was shown. (**D**, **E**). Sequence alignments of CLD of mNCAN and rat (r) ACAN (D) and FNIII-3-5 of mTNC and rTNR (E). Circles under alignments indicate the key residues of the rACAN-TNR complex. Triangles over alignments indicate the residues in the interface of mNCAN-TNC. Green and magenta circles/triangles are the residues involved in the interaction between L4 loop of CLD and βC, F, G strands of FNIII-4 and β6, 7 strands of CLD and CC' loop of FNIII-4, respectively. Black circles/triangles indicate residues involved in the interaction between CLD and FNIII-4-5 linker region/FG loop of FNIII-5.

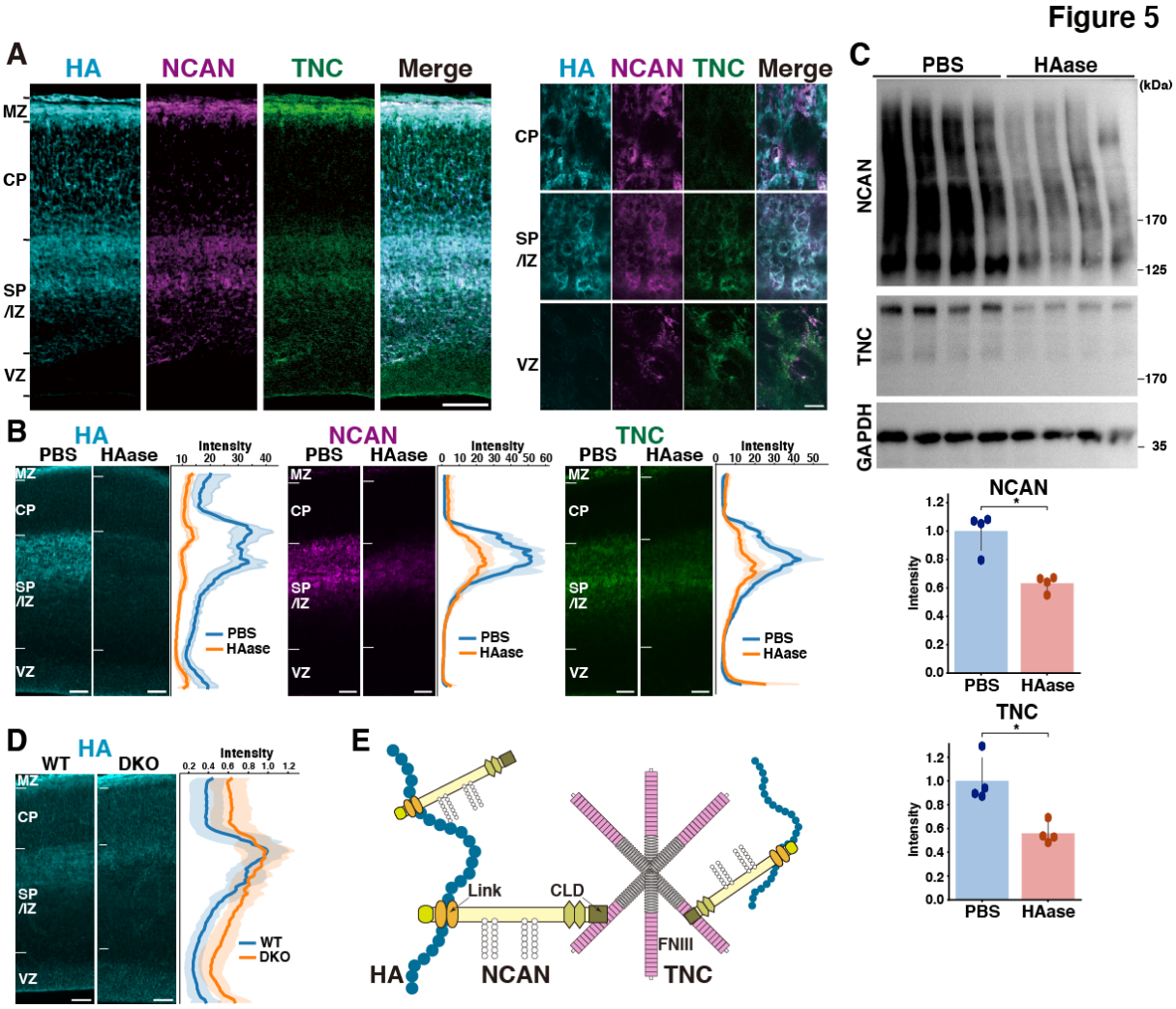

Fig. 5. HA, NCAN, and TNC from the ternary complex in the developing cerebral cortex.

(**A**) Triple staining of the E17 mouse cerebral cortex with HA (cyan), NCAN (magenta), and TNC (green). Right panels are high magnification images showing the co-localization of the three components in the upper part of the SP/IZ, but not in the CP or VZ. (**B**) Localization of HA, NCAN, and TNC in the cerebral cortex two days after an intraventricular injection of PBS or hyaluronidase (HAase) at E14. The normalized fluorescence intensity profiles of HA, NCAN, and TNC are shown on the right of each image. N = 5 mice for each group. Mean ± SD (shaded area). (**C**) Immunoblot analysis of NCAN and TNC in cerebral cortex lysates two days after an intraventricular injection of PBS or HAase. Protein levels were represented relative to the PBS-injected group. N = 4 mice per group. Mean ± SD; *p < 0.01; the Student's *t*-test. (**D**) Distribution patterns of HA in the E16 cerebral cortex of WT and DKO mice. The fluorescence intensity profile is shown on the right. N = 11 mice for each group. Mean ± SD (shaded area). (**E**) Model for forming the ternary complex of NCAN, HA, and TNC. Scale bars represent 100 μm (left panels in A), 5 μm (right panels in A), and 50 μm (B, D).

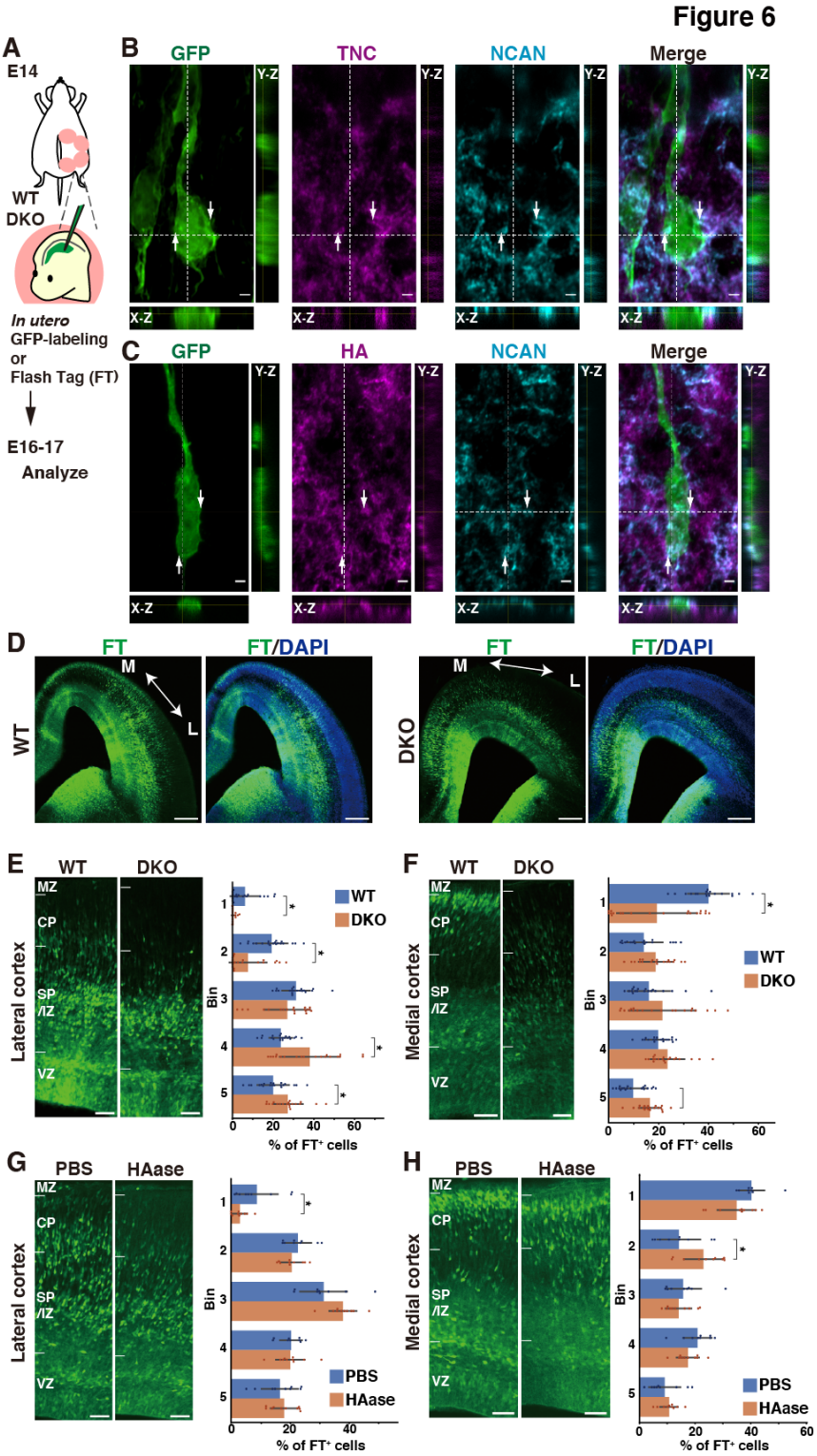

Fig. 6. Disruption of the ternary complex retards neuronal migration.

(**A**) Experimental model for *in utero* cell labeling. (**B, C**) Localization of TNC (B, magenta), NCAN (B, C, cyan), and HA (C, magenta) around GFP-labeled bipolar neurons (green) in the upper SP/IZ at E17, three days after *in utero* labeling. Orthogonal views taken along the white dashed lines showed the contact between the ternary complex and the surface of bipolar neurons,

as indicated by the arrows. (**D**) Low magnification images of FT-labeled cells (green) in WT and DKO mouse coronal sections at E16. Nuclei were counterstained with DAPI (blue). M: medial; L: lateral. (**E, F**) Radial distribution of FT-labeled cells (green) in the lateral (E) and medial (F) cortex of WT and DKO mice at E16. A quantitative analysis of migration profiles across the cortex is shown on the right. The cerebral cortex is divided into five equal areas (bins 1–5) from the pia to the ventricle, and the proportion of FT-labeled cells in each bin was calculated. N = 19–20 mice per group. Mean ± SD; *p < 0.05; the Student's *t*-test. (**G, H**) Distribution of FT-labeled cells (green) in the lateral (G) and medial (H) cortices two days after an injection of PBS or hyaluronidase (HAase) at E14. Migration profiles were analyzed as in (E, F). N = 9–10 mice per group. Mean ± SD; *p < 0.05; the Student's *t*-test. Scale bars represent 2 μm (B), 200 μm (D), and 50 μm (E-H).

Figure 7

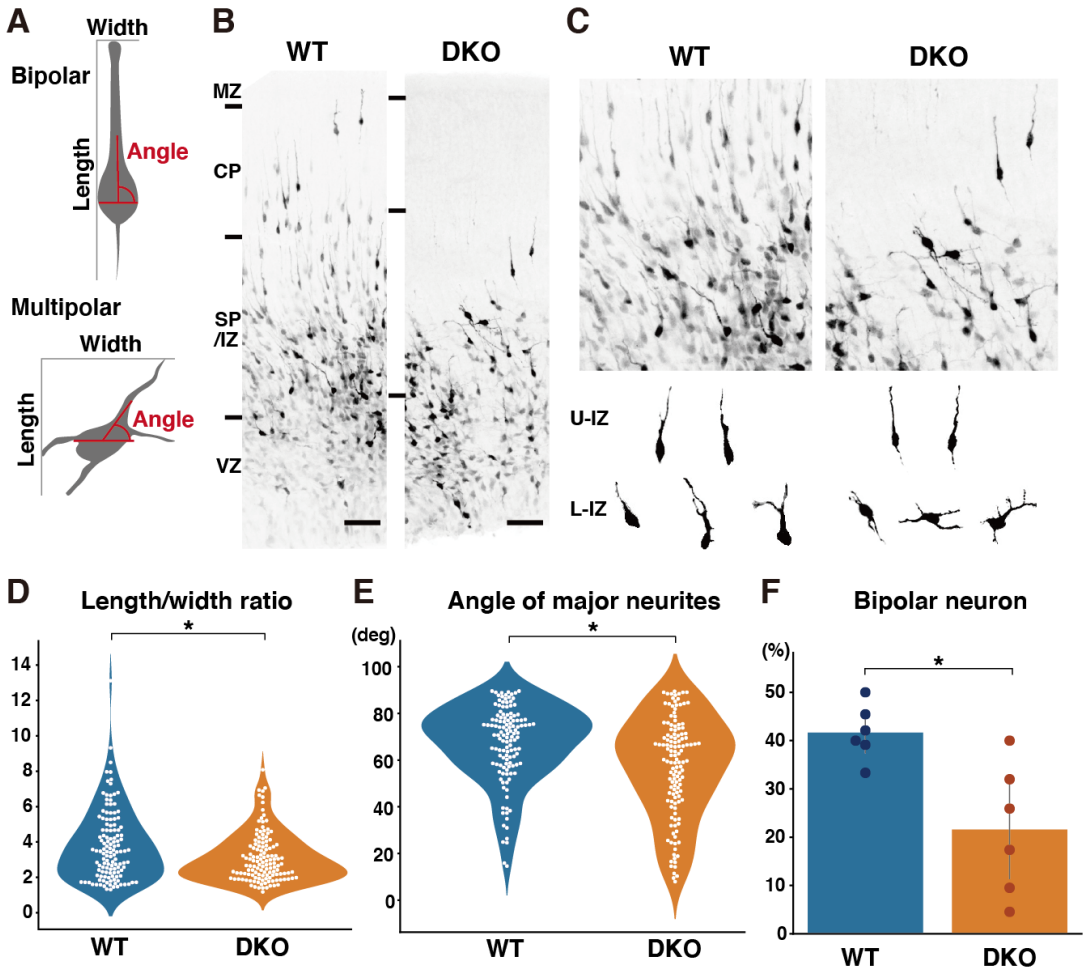

Fig. 7. Delayed multipolar-to-bipolar transition in DKO mice.

(**A**) Schematic of the morphological analysis. (**B, C**) Migration of mCherry-labeled cells in the WT and DKO cerebral cortices at E16, 53 h after *in utero* labeling (B). High magnification images (C) of mCherry-labeled cells in the IZ. The images below show the morphology of neurons in the upper-IZ (U-IZ) and lower-IZ (L-IZ). (**D, E**) The length-to-width ratio (E) and the major neurite angle (F) of mCherry^{+} neurons in WT and DKO mice. N = 128–134 cells from 6 mice per group. Mean ± SD; *p < 0.05; the Student's *t*-test. (**F**) The proportion of bipolar neurons among mCherry-labeled neurons in the WT and DKO cortices. N = 6 mice per group. Mean ± SD; *p < 0.05; the Student's *t*-test. Scale bars represent 50 μm (B).

Figure 8

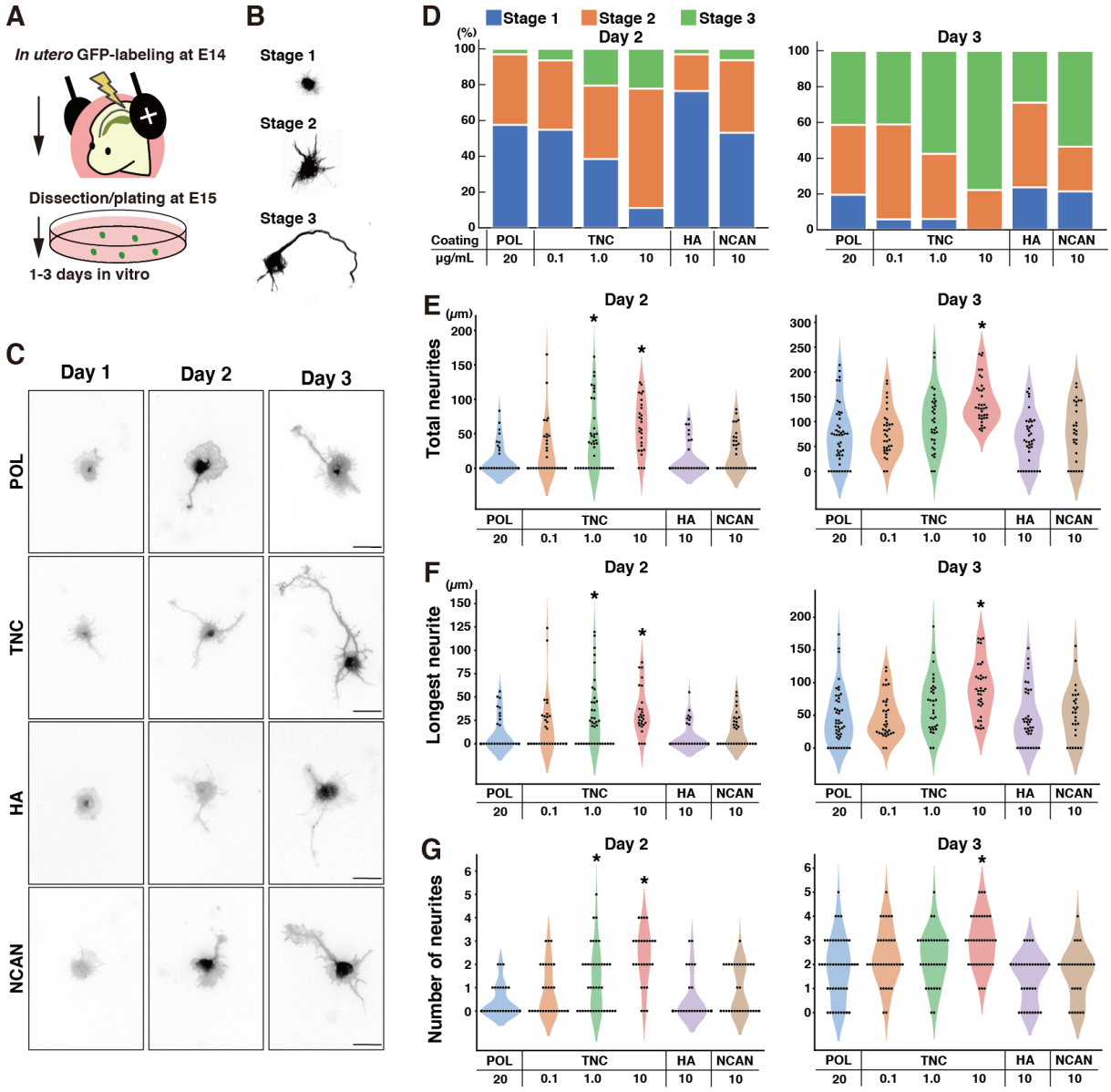

Fig. 8. TNC promotes the neurite outgrowth and morphological maturation of cortical neurons.

(**A**) Experimental model for *in utero* cell labeling and the primary culture. (**B**) Morphological stages of primary cultured cortical neurons. (**C**) Representative images of GFP-labeled neurons cultured for 1 to 3 days on cover glasses coated with the control substrate, poly-L-ornithine (POL), and 10 μg/mL of TNC, HA, and NCAN. (**D**) The percentage of neurons with each morphological stage after culturing on the indicated substrate for 2 and 3 days. (**E-G**) The total length of neurites (E), length of the longest neurite (F), and the number of neurites (G) of neurons cultured on the indicated substrate for 2 and 3 days. N = 28–46 cells per condition. Mean ± SD; *$p < 0.05$ vs POL; Dunnett's test. Scale bars represent 20 μm.

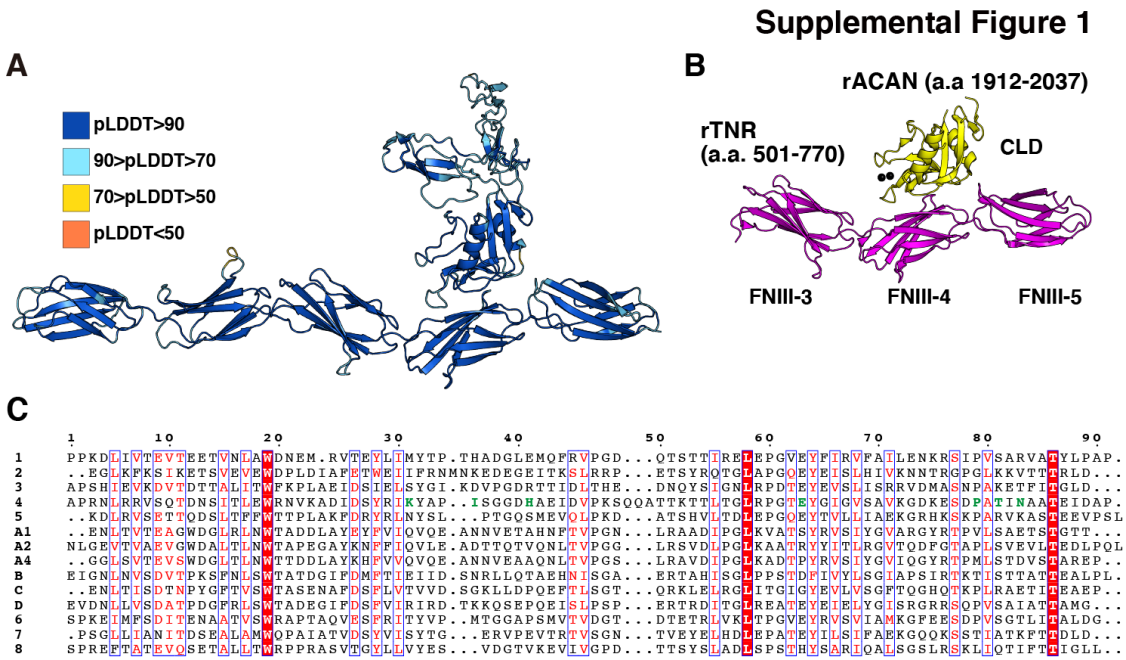

Supplemental Fig. 1. Alphafold2 prediction of NCAN-TNC complex.

(**A**) Model confidence of NCAN-TNC complex. Each residue is colored by pLDDT score, and high pLDDT score indicates high accuracy. (**B**) Crystal structure of rat (r) ACAN-TNR complex (PDB ID: 1TDQ). Each domain is colored the same as in Fig. 4C. (**C**) Sequence alignments of fourteen FNIII of mTNC. Green letters indicate residues involved in the interaction between FNIII-4 and CLD of NCAN.

Supplemental Figure 2

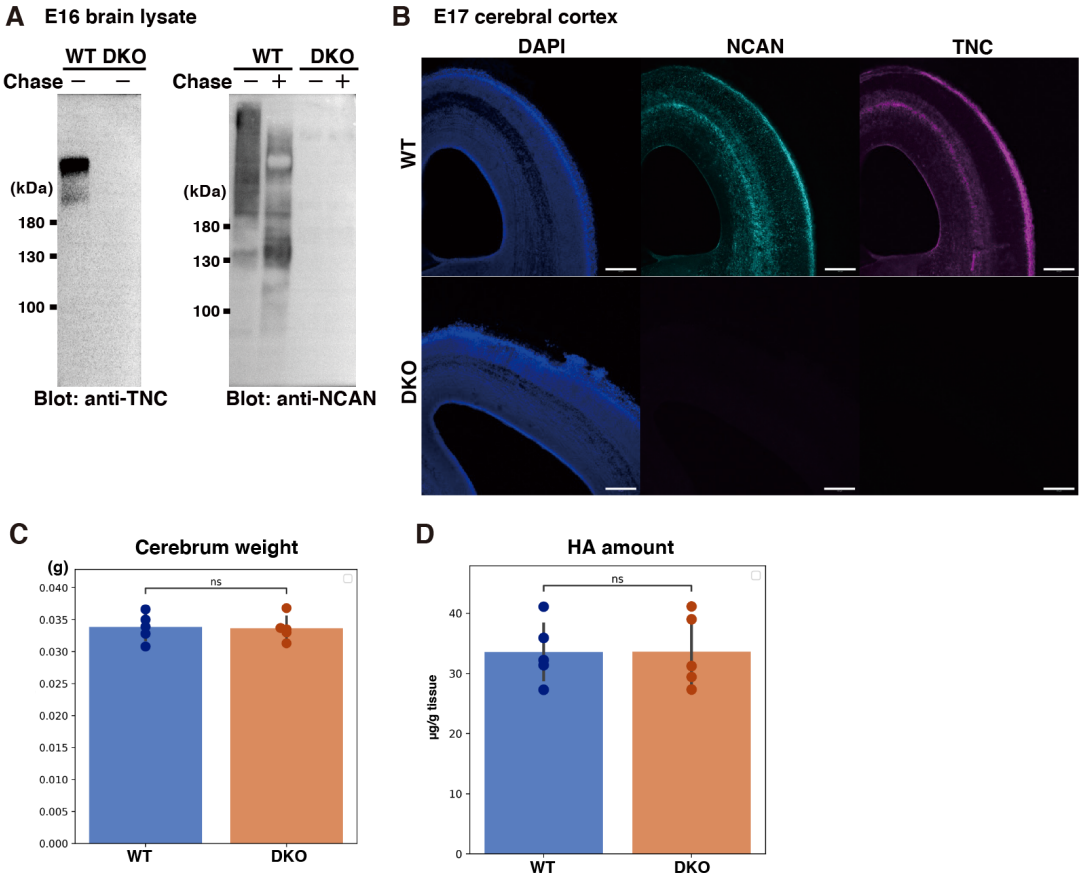

Supplemental Fig. 2. Characterization of double knockout (DKO) mice for NCAN and TNC.

(**A**) Immunoblot analysis of TNC and NCAN from WT and DKO mouse cerebral cortex lysates digested with or without chondroitinase ABC (Chase). (**B**) Immunostaining of NCAN and TNC on coronal sections of WT and DKO mouse brains at E17. Scale bars represent 200 μm. (**C**) No significant difference in cerebrum weights between WT and DKO mice at E16. N = 5 mice per group. Mean ± SD; ns > 0.05; the Student's *t*-test. (**D**) No significant difference in the amount of HA in the cerebrum between WT and DKO mice at E16. N = 5 mice per group. Mean ± SD; ns > 0.05; the Student's *t*-test.

Supplemental Figure 3

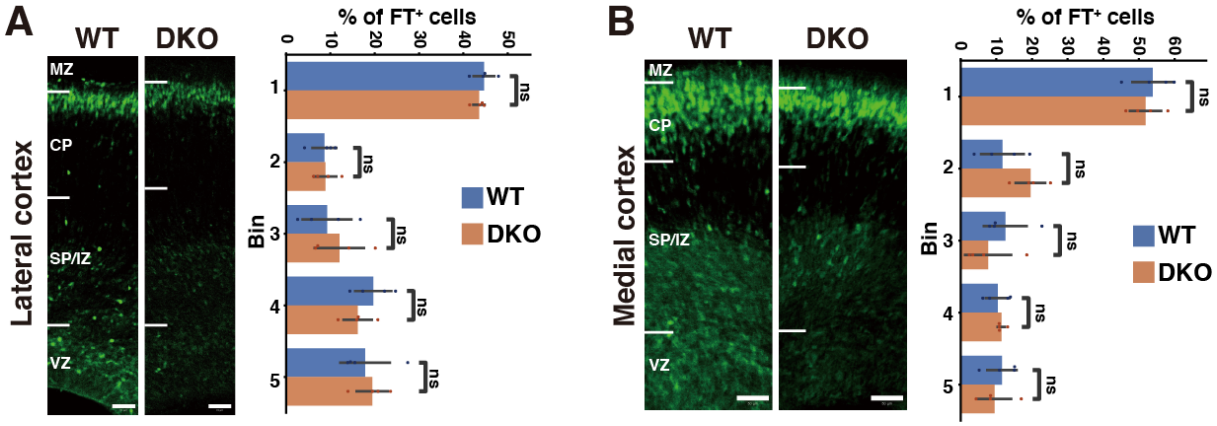

Supplemental Fig. 3. Restored neuronal migration in DKO mice after three days of labeling. (**A, B**) Radial distribution of FT-labeled cells (green) in the lateral (A) and medial (B) cortices of WT and DKO mice at E17. A quantitative analysis of migration profiles across the cortex is shown on the right. N = 4 mice per group. Mean ± SD; ns > 0.05; the Student's *t*-test. Scale bars represent 50 µm.

Supplemental Figure 4

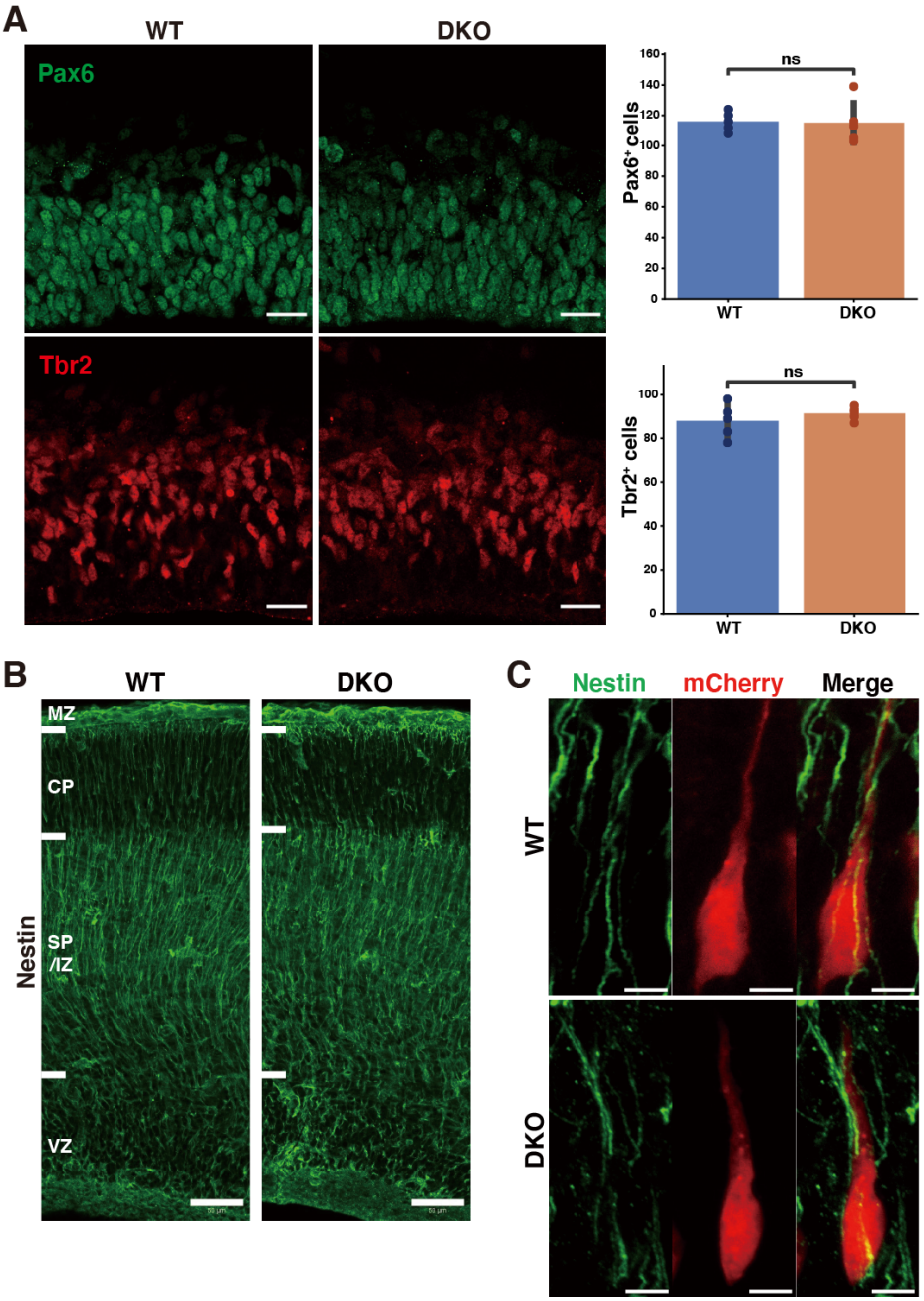

Supplemental Fig. 4. Histochemical analysis of radial glial cells, intermediate progenitor cells, and the morphology of radial fibers.

(**A**) Immunostaining of Pax6-positive radial glial cells and Tbr2-positive intermediate progenitor cells in the VZ of WT and DKO cerebral cortices at E16. Bar graphs show the numbers of Pax6- and Tbr2-positive cells per 150 × 150 μm^2. N = 5 mice per group. Mean ± SD; ns > 0.05; the Student's *t*-test. (**B**) Immunostaining of nestin-positive radial fibers in WT and DKO cerebral cortices at E16. (**C**) High magnification images of mCherry-positive bipolar neurons and radial fibers in the WT and DKO at E16, 2 days after *in utero* labeling. Bipolar neurons in the SP/IZ-attached radial fiber, irrespective of genotypes. Scale bars represent 20 μm (A), 50 μm (B), and 5 μm (C).

Supplemental Figure 5

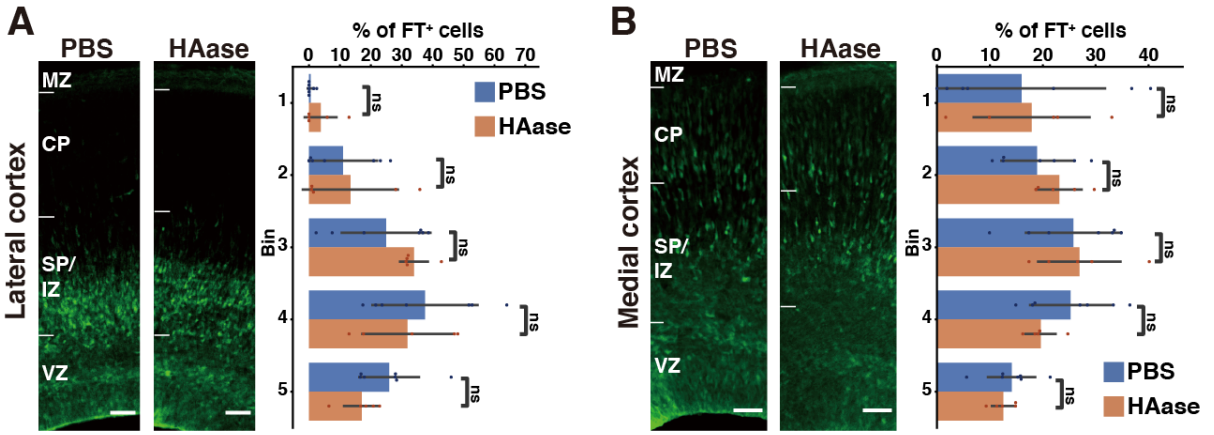

Supplemental Fig. 5. The digestion of HA in DKO mice does not further affect neuronal migration. (**A, B**) Distribution of FT-labeled cells (green) in the lateral (A) and medial (B) cortices of DKO mice two days after an injection of PBS or hyaluronidase (HAase) at E14. A quantitative analysis of migration profiles across the cortex is shown on the right. N = 5–7 mice per group. Mean ± SD; ns > 0.05; the Student's *t*-test. Scale bars represent 50 µm.

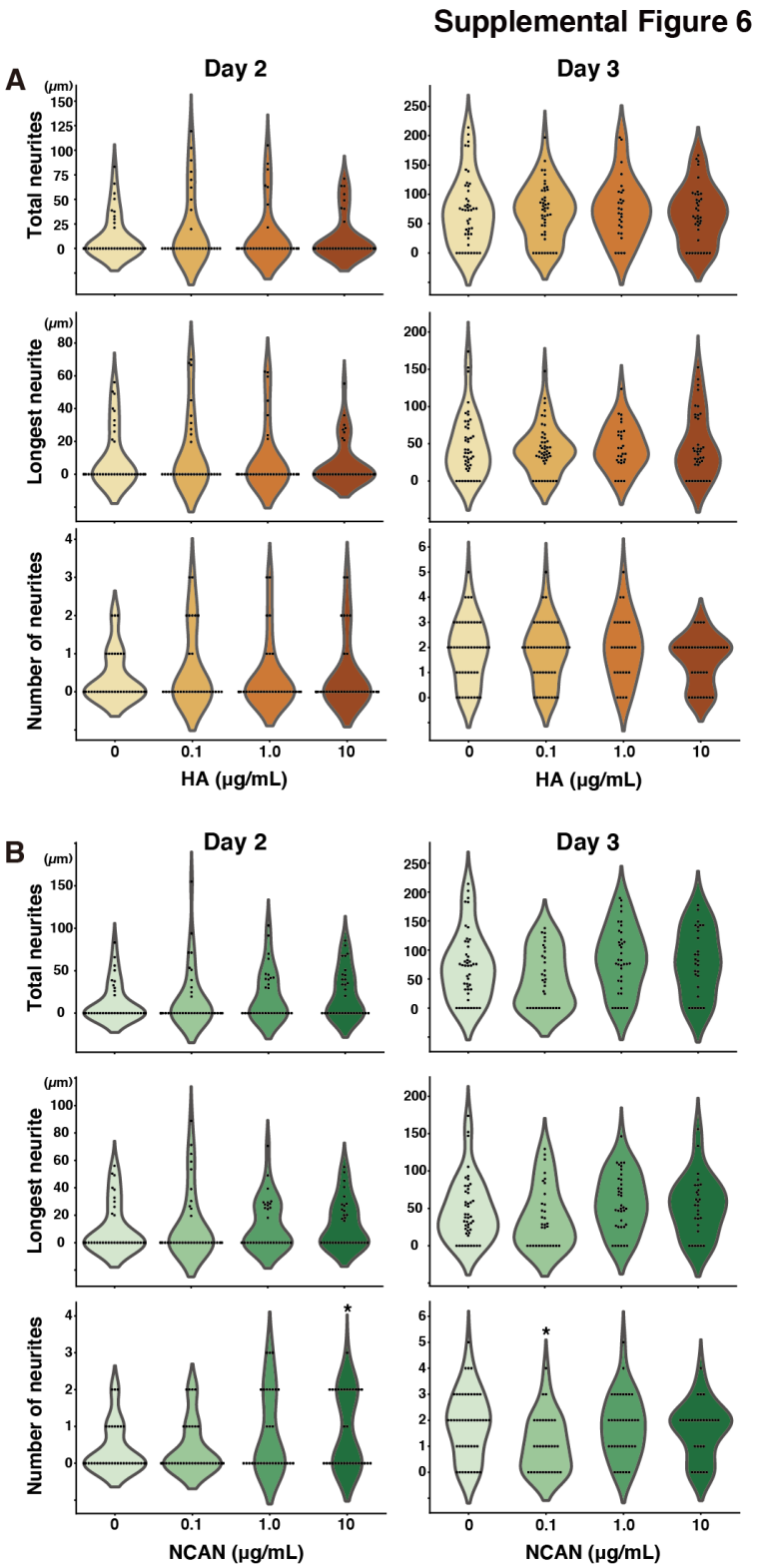

Supplemental Fig. 6. Culturing neurons on HA and NCAN does not affect the length of neurites. (**A, B**) The total length of neurites (upper panels), the length of the longest neurites (middle panels), and the number of neurites of neurons (lower panels) cultured on cover glasses coated with the indicated concentrations of HA (A) and NCAN (B) for 2 and 3 days. N = 28–46 cells per condition. Mean ± SD; *p < 0.05 vs 0 μg/mL; Dunnett's test.

Acknowledgments

This research was funded by the Ministry of Education, Culture, Sports, Science & Technology, Japan [grant number 15K21067, 18K06130, and 21H05681 to S.M.] and the LOTTE Foundation [grant name Lotte Shigemitsu Prize to S.M.]. The authors thank Takeshi Kawauchi for valuable discussion, Makoto Matsuyama for technical advice on i-Gonad, Hitoshi Mori for technical assistance in mass spectrometry, and Hidekazu Takahashi for launch of a computational system for protein structure prediction. pCAG-GFP and pCAG-mGFP (Addgene plasmid # 11150 and #14757) were a gift from Connie Cepko. We thank the RIKEN Bioresource Center for *Tnc*-deficient mice (RBRC00169).

Author contributions

A.M., M.T., and S.M. designed research and conducted experiments. S.N. and T.M. contributed to mass spectrometry and protein structure prediction. C.S., K.K., H.K., and S.M. contributed to the biochemical analysis of NCAN and HA. C.S., K.K., T.M., H.K., and S.M. interpreted data. A.M., S.N., and S.M. wrote the draft and all authors revised and approved the final manuscript.

Declaration of interests

The authors declare no competing interests.

Materials and Methods

Mice used in the present study

All animal experimental studies were conducted with the approval of the Committee on Animal Experiments of the Graduate School of Bioagricultural Sciences, Nagoya University, and Tokyo University of Agriculture and Technology. Pregnant ICR (RRID:MGI:5462094) and C57BL/6NCrSlc (RRID:MGI:5295404) mice were purchased from Japan SLC (Shizuoka, Japan). *Tnc*-deficient mice on a C57BL/6NJcl background were obtained from the RIKEN Bioresource Center (BRC No. RBRC00169)[64]. *Ncan*-deficient mice were generated using CRISPR-Cas9-based improved genome editing via oviductal nucleic acids delivery (i-GONAD)[65,66]. A guide RNA targeting the mouse *Ncan* loci (Mm.Cas9.NCAN.1.AA: 5'-ACCTTAGTCCACTTGATCCGAGG-3') was chosen from Predesigned Alt-R CRISPR-Cas9 guide RNA on the Integrated DNA Technologies (IDT) website (https://sg.idtdna.com). Synthetic crRNAs, tracrRNA, and Cas9 Nuclease V3 were purchased from IDT. Surgical procedures for i-GONAD were performed under deep anesthesia at approximately 3 pm on the day on which a vaginal plug was detected. A mixture of 30 μM crRNA/tracrRNA complex and 1 mg/mL Cas9 Nuclease V3 was prepared in PBS. Approximately 2.5 μL of the mixture was injected into the oviduct upstream of the ampulla using a glass micropipette. The oviduct was clasped with a paired electrode (CUY652P2.5X4, NEPA Gene). Square electric pulses (poring pulse: 50 V, 5-ms pulse, 50-ms pulse interval, 3 pulses, 10% decay, ± pulse orientation, and transfer pulse: 10 V, 50-ms pulse, 50-ms pulse interval, 3 pulses, 40% decay, ± pulse orientation) were passed using an electroporator (NEPA21, NEPA Gene). Offspring were genotyped by DNA sequencing to identify founder animals. After

first mating with *Tnc*-deficient mice, the F1 generation was sequenced and further crossed to *Tnc*-deficient mice in order to obtain DKO mice.

Cell lines used in the present study

The HEK293 (RCB1637) cell line was obtained from the Riken Cell Bank (Tsukuba, Japan) and used for protein pull-down experiments.

Immunoblotting

Mouse brains were homogenized in PBS containing 1% Triton X-100 and protease inhibitor cocktail (Sigma) and incubated on ice for 30 min. After centrifugation at 15,000 × g at 4°C for 30 min, the protein concentrations of supernatants (brain lysates) were assessed using a BCA assay kit (Thermo). Regarding chondroitinase ABC digestion, the brain lysate (70 μg as protein) was digested with 5 milliunits of protease-free chondroitinase ABC (Sikagaku Corp) at 37°C for 1 h. Digested and undigested lysates were denatured with 2% sodium dodecyl sulfate (SDS) and 5% mercaptoethanol at 95°C for 5 min. Proteins were separated using 6 or 10% SDS-polyacrylamide gel electrophoresis (PAGE) and transferred to polyvinylidene difluoride membranes. After blocking with 2% skim milk in PBS containing 0.1% Tween-20 (PBST), the membranes were incubated with an antibody recognizing the neoepitope of CSPGs (mouse, 1:50000, Millipore), anti-NCAN (sheep, 1:3000, R&D), anti-glyceraldehyde 3-phosphate dehydrogenase (GAPDH) (mouse, 1:10000, Wako), anti-TNC (rat, 1:3000, R&D), and anti-GFP (rabbit, 1:3000, MBL) at 4°C overnight. After washing, the membranes were incubated with appropriate horseradish peroxidase (HRP)-conjugated secondary antibodies (1:2500) at room temperature for 1 h. Signals were detected with Immobilon Western Chemiluminescent HRP Substrate (Millipore) and imaged on a LuminoGraph I (ATTO).

Histochemistry

Mouse embryos were transcardially perfused with PBS, followed by 4% paraformaldehyde in PBS. Brains were removed and post-fixed overnight with 4% paraformaldehyde in PBS. Coronal sections (thickness of 80 μm) were cut with the vibratome VT1200 (Leica). Sections were permeabilized with 0.25% Triton X-100 in PBS and then blocked with PBST containing 2% bovine serum albumin (Sigma). Sections were incubated at 4°C overnight with biotinylated HA-binding protein (b-HABP) (1:400, Hokudo), anti-NCAN (sheep, 1:400, R&D), anti-TNC (rat, 1:400, R&D), anti-Pax6 (rabbit, 1:400, Invitrogen), anti-Tbr2 (mouse, 1:400, Wako), anti-Nestin (mouse, 1:400, Millipore), and Alexa Fluor 488-conjugated anti GFP (rabbit, 1:1000, Invitrogen). After washing, sections were incubated with the appropriate Alexa Fluor conjugate secondary antibody and streptavidin (Thermo), followed by cell nuclear staining with DAPI (0.1 μg/mL). Images were captured with the AX R confocal microscope (Nikon) or LSM 710 NLO confocal microscope (Carl Zeiss). In a three-dimensional reconstruction, images were captured using the Z-stack function of the confocal microscope, and Z-projection and orthogonal views were obtained by ImageJ FIJI software.

Quantitative reverse transcription (RT)-PCR

Total RNA from the developing mouse cerebral cortex and isolated GFP-positive cells were prepared using the RNeasy mini kit (Qiagen). cDNA was synthesized using SuperScript III reverse transcriptase (Thermo). Real-time RT-PCR was performed with the PowerUp SYBR Green Master Mix (Thermo) in the StepOne PCR system (Thermo). All primers used are listed in the Key Resources table. Relative gene expression was calculated using the comparative cycle threshold (Ct) method. Expression levels were normalized to *Gapdh*.

***In situ* hybridization**

Target sequences detecting *Ncan* and *Tnc* were amplified from mouse brain cDNA and cloned into the pSPT 19 vector (Roche). All primers used for probe amplification are listed in the Key Resources table. Digoxigenin (DIG)-labeled sense and antisense probes were generated with T7 and Sp6 RNA polymerase using a DIG RNA labeling kit (Roche) according to the manufacturer's instructions. RNA probes were purified with the RNeasy Mini Kit (Qiagen) and quantified using a Nanodrop (Thermo Fisher Scientific). ICR mouse embryos were removed from pregnant females at E16 and perfused with 4% paraformaldehyde in PBS. Brains were post-fixed overnight with 4% paraformaldehyde in PBS and embedded in OCT compound (Sakura Finetek). Frozen sections were cut coronally with a Leica Jung CM3000 cryostat (Leica) at a thickness of 20 μm. Brain sections were fixed with 4% paraformaldehyde in PBS, treated with 1 μg/mL proteinase K, permeabilized with 0.3% Triton X-100 in PBS, and hybridized with 0.5 μg/mL DIG-labeled probes at 70°C overnight in a moist chamber. After washing three times with 0.2 × saline-sodium citrate at 70°C for 30 min, sections were blocked with 10% blocking reagent (Roche) at room temperature for 1 h and incubated with alkaline phosphatase-conjugated anti-DIG antibody (Roche) overnight at 4°C. The hybridization signal was developed with NBT/BCIP solution (Roche).

Identification of the 130-kDa band by MALDI-TOF/TOF

Ten E18 mouse brains were homogenized in 10 mL of Hanks' Balanced Salt Solution (Gibco) containing 1% Triton X-100, 10 mM HEPES (pH 7.6) (Gibco), and protease inhibitor cocktail (Sigma) and incubated on ice for 1 h. After centrifugation at 15,000 × g at 4°C for 30 min, the supernatant was applied to a DEAE-Toyopearl 650 M column (1 mL, Tosoh) equilibrated with buffer A (0.1% Triton X-100, 10 mM Tris–HCl, pH 7.5). The column was washed with buffer A containing 0.25 M NaCl and then eluted with buffer A containing 0.5 M NaCl. The eluent was diluted with a four-fold volume of buffer A and digested with 50 milliunits of chondroitinase ABC (Sikagaku Corp) at 37°C for 4 h. The digest was again applied to a DEAE-Toyopearl 650 M column (0.4 mL) and eluted with buffer A containing 0.25 M NaCl. The eluent was applied to a heparin-agarose column (0.3 mL, Sigma), and the flow-through fraction was collected. After ultrafiltration with the YM-10 membrane (Amicon), the concentrate was separated using 6% SDS-PAGE. After staining with Coomassie Brilliant Blue, the 130-kDa band was cut out as a gel piece and digested with trypsin (Promega) at 37°C overnight. The recovered tryptic peptides were subjected to nano-LC (DiNa Nano LC system, KYA Technologies), and eluted fractions were spotted on the MALDI plate (AB SCIEX) with α-

cyano-4-hydroxyciccanic acid (Shimadzu) as a matrix using the Direct nano LC/MALDI Spotter (KYA technologies). Peptides were analyzed for identification using a MALDI mass spectrometer (TOF/TOF 5800, AB SCIEX). MS/MS data were analyzed using MASCOT software (Matrix Science) as previously described[67].

Pull-down assay for HA-binding molecules

One hundred microliters of the E16 mouse brain lysate was digested with 1 unit of hyaluronidase from *Streptomyces hyalurolyticus* (Sigma) at 37°C for 1 h. Digested and undigested samples were incubated with 1.25 μg of b-HABP (Hokudo) or 0.25 ng of biotinylated HA (b-HA) (PG research) at 4°C overnight, followed by precipitation by mixing with 25 μL streptavidin-coupled magnetic beads (Thermo) at room temperature for 1 h. After washing the precipitates with PBST, the supernatant and precipitates were digested with 5 milliunits of chondroitinase ABC (Sikagaku Corp) at 37°C for 2 h, denatured by SDS at 95°C for 5 min, and then analyzed by immunoblotting, as described above.

Quantification of HA

Cerebrum lysates were prepared from E16 WT and DKO mice as described above. HA concentrations in the lysates were measured by enzyme-linked immunosorbent assays (ELISA) as previously reported[68]. Briefly, each well of a 96-well plate (Iwaki) was coated with 0.1% HABP (Cosmo-bio) at 4°C overnight. After washing with PBST, each well was blocked with 1% BLOCK ACE (KAC) in PBS at 37°C for 2 h, followed by an incubation with 1 mg/mL HA (Wako) in the blocking solution at 37°C for 1 h. After washing, a mixture of 0.05% b-HABP (Hokudo) and the cerebrum lysates was added to each well and incubated at 37°C for 1 h. b-HABP was detected by HRP-conjugated streptavidin (1:25000, Wako) and ELISA POD Substrate TMB (Nacalai Tesque).

Construction of NCAN-expressing plasmids

We amplified the full-length *Ncan* sequence by PCR from the mouse brain cDNA library and assembled it into the pCAG-GFP vector using the NEBuilder HiFi DNA Assembly Master Mix (New England Biolabs) or In-Fusion HD Cloning Kit (TaKaRa). The GFP-fused full-length NCAN-expressing plasmid was constructed by inserting the fragment encoding GFP amplified from the pCAG-GFP vector into the central region of NCAN (corresponding to Val641 to Leu644). The plasmids expressing the N- and C-terminal halves of NCAN were constructed by deleting the C-terminal and N-terminal regions from full-length NCAN using the KOD-Plus Mutagenesis Kit (Toyobo).

Identification of NCAN interactors by a LC-MS/MS analysis

HEK293 cells were transfected with plasmids expressing GFP-fused NCAN using Lipofectamine 3000 reagent (Thermo). After three days, recombinant proteins were isolated from the culture medium using GFP-Trap agarose (Chromotek, Martinsried, Germany). GFP fused-NCAN immobilized to agarose was incubated

with embryonic mouse brain lysates at 4°C overnight. After washing with PBST, precipitated proteins were denatured with 8 M urea, subjected to reductive alkylation by dithiothreitol and iodoacetamide, and then digestion by trypsin (Promega). The resultant peptide fragments were analyzed using the LC-MS/MS system (QTRAP5500, AB Sciex) as previously described[67,69].

Structure prediction using AlphaFold2

Based on the previous rACAN-TNR complex structure (PDB ID 1TDQ)[36], we selected the amino acid sequences of the C-terminal part of mNCAN (T961-I1224) and FNIII-1-5 of mTNC (S624-E1073). We generated five complex models using AlphaFold2 multimer (v2)[70] implemented in ColabFold[71]. ColabFold ran with default parameters. All structures are visualized using PyMOL v.2.5.0 (Schrödinger, LLC).

Sequence alignment

Alignments were generated using MAFFT[72] and visualized using ESPript3[73]. Amino acid residues involved in the interface region of the predicted mNCAN-TNC complex were analyzed using PDBsum[74] or Protein Interactions Calculator (PIC) webserver[75].

Intraventricular injection of hyaluronidase

Pregnant WT and DKO mice were anesthetized with isoflurane (3% for induction and 2% for maintenance) using an animal anesthetizer (Muromachi) during the whole surgery. Between 1 and 2 μL of hyaluronidase from *S. hyalurolyticus* (1 unit/μl, Sigma) or PBS was injected into the lateral ventricle using a pulled glass capillary. Fast Green dye (Wako) was co-injected to visualize successful injections with hyaluronidase. After injections, the uterine horns were placed back into the abdominal cavity to allow further embryonic growth. Coronal sections (thickness of 80 μm) were prepared 2 days after injections and analyzed histochemically to detect HA, NCAN, and TNC as described above. Regarding staining intensity profiles, a 50-μm-wide area spanning the CP to VZ was divided into 100 equal bins and the fluorescence intensity of each region was assessed.

Neuronal migration analysis by Flash Tag (FT)[37,39]

1 mM carboxyfluorescein succinimidyl ester (Dojindo) in PBS with or without 1 unit *S. hyalurolyticus* hyaluronidase (Sigma) was injected into the lateral ventricle using a pulled glass capillary at E14. After 2 or 3 days, coronal sections (thickness of 80 μm) were prepared, and fluorescent images were captured as described above. The top 10% of cells with high fluorescence intensity were extracted and analyzed using ImageJ FIJI. The cerebral cortex was divided into five equal areas (bins 1–5) from the pia to the ventricle, and the proportion of FT-labeled cells in each bin was calculated.

***In utero* electroporation**

WT and DKO mouse embryos at E14 or E15 were electroporated *in utero* to label neural progenitor cells in

the VZ, as previously described[28,76]. Pregnant mice were initially anesthetized with isoflurane (3% for induction and 2% for maintenance) using an animal anesthetizer (Muromachi) during surgery. Between 1 and 2 microliters of 1 μg/μL plasmid solution was injected into the lateral ventricle using a pulled glass capillary. The head was clasped with a paired electrode (CUY650P5, NEPA Gene), and square electric pulses (33 V for 50 ms, five times in 950-ms intervals) were passed using an electroporator (NEPA21, NEPA Gene). After electroporation, the uterine horns were placed back into the abdominal cavity to allow further embryonic growth.

Isolation of migrating neurons from the cerebral cortex

GFP labeling followed by cell sorting was performed as previously reported[28]. Briefly, neural progenitor cells in the VZ of the cerebral cortex at E14 were transfected with pCAG-GFP using *in utero* electroporation as described above. Embryonic brains were harvested 0.6–4 days later, and GFP-positive regions were dissected from the cerebral cortices under a fluorescence stereomicroscope (Leica). Cortical fragments were incubated in 0.25% trypsin and mechanically dispersed by gentle pipetting to dissociate single cells. GFP-positive cells were isolated from the single-cell suspension by sorting using a JSAN fluorescence-activated cell sorter (Bay Bioscience).

Morphological analysis of cortical neurons

Neural progenitor cells in the VZ were transfected with pCAG-mCherry by *in utero* electroporation at E14. After 53 h, coronal sections (thickness of 80 μm) were prepared, and fluorescent images were captured as described above. Neuronal morphology was evaluated by measuring the length-to-width ratio of labeled neurons and the angle between major neurites and the ventricle surface using ImageJ FIJI. Bipolar neurons were defined as cells with a length-to-width ratio greater than three and an orientation angle greater than 70°.

Primary cultured cortical neurons

Cover glasses were pre-coated with 20 μg/mL poly-L-ornithine (PLO) (Wako) at 37°C overnight and then overlaid with 0.1–10 μg/mL of recombinant human TNC (R&D), recombinant human NCAN (R&D), and HA (600–1200 kDa, PG research) at 37°C for 3 h. Embryonic brains were harvested 24 h after *in utero* electroporation with pCAG-GFP at E14 or E15[77]. GFP-positive regions were dissected from the cerebral cortices under a fluorescence stereomicroscope (Leica). Cortical fragments were incubated in 20 units/mL papain (Worthington Biochemical Corporation) and mechanically dispersed by gentle pipetting. Dissociated cells were plated on ECM-coated cover glasses at a density of 50,000 cells per well (1.9 mm^2). Cells were maintained for 1 to 3 days in Neurobasal Plus Medium (Thermo) supplemented with 2% B-27 Plus (Thermo), 5% horse serum (Sigma), and antibiotics (Thermo). Cultures were fixed with 4% paraformaldehyde, stained with an Alexa 488-conjugated anti-GFP antibody (Thermo) and anti-Tuj (mouse, 1:1000, Sigma), and imaged as described above. Processes longer than 10 μm were measured as neurites using NeuronJ[78]. Neurons without neurites were classified as stage 1, neurons with neurites shorter than 50 μm as stage 2, and neurons

with neurites longer than 50 μm as stage 3. Regarding immunoblotting in Fig. 1I and immunostaining in Fig. 2D, dissociated cells were plated on PLO-coated cover glasses at 200,000 and 50,000 cells per well, respectively.

Quantification and statistical analysis

All data are presented as the mean ± SD. Statistical analyses were performed using Python within the Jupyter Notebooks environment and Easy R[79]. An unpaired, two-tailed Student's *t*-test was used to compare results from two groups. Dunnett's test was used to compare multiple experimental groups against the control group. A p value <0.05 was considered to be significant. Details of statistical analyses, including the statistical tests used, N values, and p values, may be found in the relevant figures and/or figure legends.

References

1. Kriegstein, A. R. & Noctor, S. C. Patterns of neuronal migration in the embryonic cortex. *Trends in Neurosciences* **27**, 392–399 (2004).
2. Barnes, A. P. & Polleux, F. Establishment of axon-dendrite polarity in developing neurons. *Annu. Rev. Neurosci.* **32**, 347–381 (2009).
3. Taverna, E., Götz, M. & Huttner, W. B. The Cell Biology of Neurogenesis: Toward an Understanding of the Development and Evolution of the Neocortex. *Annu. Rev. Cell Dev. Biol.* **30**, 465–502 (2014).
4. Kriegstein, A. & Alvarez-Buylla, A. The glial nature of embryonic and adult neural stem cells. *Annu Rev Neurosci* **32**, 149–184 (2009).
5. Noctor, S. C., Martínez-Cerdeño, V., Ivic, L. & Kriegstein, A. R. Cortical neurons arise in symmetric and asymmetric division zones and migrate through specific phases. *Nat Neurosci* **7**, 136–144 (2004).
6. Tabata, H. & Nakajima, K. Multipolar migration: the third mode of radial neuronal migration in the developing cerebral cortex. *J Neurosci* **23**, 9996–10001 (2003).
7. Namba, T. *et al.* Pioneering Axons Regulate Neuronal Polarization in the Developing Cerebral Cortex. *Neuron* **81**, 814–829 (2014).
8. Jossin, Y. & Cooper, J. A. Reelin, Rap1 and N-cadherin orient the migration of multipolar neurons in the developing neocortex. *Nat Neurosci* **14**, 697–703 (2011).
9. Hatanaka, Y. & Yamauchi, K. Excitatory Cortical Neurons with Multipolar Shape Establish Neuronal Polarity by Forming a Tangentially Oriented Axon in the Intermediate Zone. *Cerebral Cortex* **23**, 105–113 (2013).
10. Ohtaka-Maruyama, C. *et al.* Synaptic transmission from subplate neurons controls radial migration of neocortical neurons. *Science* **360**, 313–317 (2018).
11. Kawauchi, T. *et al.* Rab GTPases-dependent endocytic pathways regulate neuronal migration and maturation through N-cadherin trafficking. *Neuron* **67**, 588–602 (2010).
12. Jossin, Y. Molecular mechanisms of cell polarity in a range of model systems and in migrating neurons. *Molecular and Cellular Neuroscience* 23 (2020).
13. Namba, T. *et al.* Extracellular and Intracellular Signaling for Neuronal Polarity. *Physiological Reviews* **95**, 995–1024 (2015).
14. Kawauchi, T. Cellullar insights into cerebral cortical development: focusing on the locomotion mode of neuronal migration. *Front Cell Neurosci* **9**, 394 (2015).
15. Emerling, D. E. & Lander, A. D. Inhibitors and Promoters of Thalamic Neuron Adhesion and Outgrowth in Embryonic Neocortex: Functional Association with Chondroitin Sulfate. *Neuron* **17**, 1089–1100 (1996).
16. Fukuda, T. *et al.* Immunohistochemical localization of neurocan and L1 in the formation of thalamocortical pathway of developing rats. *J. Comp. Neurol.* **382**, 141–152 (1997).
17. Hoerder-Suabedissen, A. & Molnár, Z. Development, evolution and pathology of neocortical subplate neurons. *Nat Rev Neurosci* **16**, 133–146 (2015).
18. Long, K. R. & Huttner, W. B. How the extracellular matrix shapes neural development. *Open Biol.* **9**,

180216 (2019).

19. Meyer-Puttlitz, B., Junker, E., Margolis, R. U. & Margolis, R. K. Chondroitin sulfate proteoglycans in the developing central nervous system. II. Immunocytochemical localization of neurocan and phosphacan. *Journal of Comparative Neurology* **366**, 44–54 (1996).
20. Miller, B., Sheppard, A. M., Bicknese, A. R. & Pearlman, A. L. Chondroitin sulfate proteoglycans in the developing cerebral cortex: The distribution of neurocan distinguishes forming afferent and efferent axonal pathways. *J. Comp. Neurol.* **355**, 615–628 (1995).
21. Ishii, M. & Maeda, N. Oversulfated Chondroitin Sulfate Plays Critical Roles in the Neuronal Migration in the Cerebral Cortex. *J. Biol. Chem.* **283**, 32610–32620 (2008).
22. Reinhard, J., Brösicke, N., Theocharidis, U. & Faissner, A. The extracellular matrix niche microenvironment of neural and cancer stem cells in the brain. *Int. J. Biochem. Cell Biol.* **81**, 174–183 (2016).
23. Zimmermann, D. R. & Dours-Zimmermann, M. T. Extracellular matrix of the central nervous system: from neglect to challenge. *Histochem Cell Biol* **130**, 635–653 (2008).
24. Miyata, S. & Kitagawa, H. Formation and remodeling of the brain extracellular matrix in neural plasticity: Roles of chondroitin sulfate and hyaluronan. *Biochim Biophys Acta Gen Subj* **1861**, 2420–2434 (2017).
25. Maeda, N. Proteoglycans and neuronal migration in the cerebral cortex during development and disease. *Front. Neurosci.* **9**, (2015).
26. Yamaguchi, Y. Lecticans: organizers of the brain extracellular matrix. *CMLS, Cell. Mol. Life Sci.* **57**, 276–289 (2000).
27. Miyata, S. & Kitagawa, H. Mechanisms for modulation of neural plasticity and axon regeneration by chondroitin sulphate. *Journal of Biochemistry* **157**, 13–22 (2015).
28. Takechi, M. *et al.* A pericellular hyaluronan matrix is required for the morphological maturation of cortical neurons. *Biochimica et Biophysica Acta (BBA) - General Subjects* **1864**, 129679 (2020).
29. Caterson, B. Fell-Muir Lecture: Chondroitin sulphate glycosaminoglycans: fun for some and confusion for others. *International Journal of Experimental Pathology* **93**, 1–10 (2012).
30. Miyata, S. & Kitagawa, H. Chondroitin 6-Sulfation Regulates Perineuronal Net Formation by Controlling the Stability of Aggrecan. *Neural Plasticity* **2016**, 1–13 (2016).
31. Rauch, U., Karthikeyan, L., Maurel, P., Margolis, R. U. & Margolis, R. K. Cloning and primary structure of neurocan, a developmentally regulated, aggregating chondroitin sulfate proteoglycan of brain. *Journal of Biological Chemistry* **267**, 19536–19547 (1992).
32. Ohya, T. & Kaneko, Y. Novel hyaluronidase from streptomyces. *Biochim. Biophys. Acta* **198**, 607–609 (1970).
33. Faissner, A., Roll, L. & Theocharidis, U. Tenascin-C in the matrisome of neural stem and progenitor cells. *Molecular and Cellular Neuroscience* **81**, 22–31 (2017).
34. Aspberg, A. *et al.* The C-type lectin domains of lecticans, a family of aggregating chondroitin sulfate proteoglycans, bind tenascin-R by protein-protein interactions independent of carbohydrate moiety. *Proc*

Natl Acad Sci U S A **94**, 10116–10121 (1997).

35. Rauch, U. *et al.* Mapping of a defined neurocan binding site to distinct domains of tenascin-C. *J Biol Chem* **272**, 26905–26912 (1997).
36. Lundell, A. *et al.* Structural Basis for Interactions between Tenascins and Lectican C-Type Lectin Domains. *Structure* **12**, 1495–1506 (2004).
37. Govindan, S., Oberst, P. & Jabaudon, D. In vivo pulse labeling of isochronic cohorts of cells in the central nervous system using FlashTag. *Nat Protoc* **13**, 2297–2311 (2018).
38. Telley, L. *et al.* Sequential transcriptional waves direct the differentiation of newborn neurons in the mouse neocortex. *Science* **351**, 1443–1446 (2016).
39. Yoshinaga, S. *et al.* Comprehensive characterization of migration profiles of murine cerebral cortical neurons during development using FlashTag labeling. *iScience* **24**, 102277 (2021).
40. Castello, M. A. & Gleeson, J. G. Insight into developmental mechanisms of global and focal migration disorders of cortical development. *Current Opinion in Neurobiology* **66**, 77–84 (2021).
41. Fernández, V., Llinares-Benadero, C. & Borrell, V. Cerebral cortex expansion and folding: what have we learned? *EMBO J* **35**, 1021–1044 (2016).
42. Chen, G. *et al.* Semaphorin-3A guides radial migration of cortical neurons during development. *Nat Neurosci* **11**, 36–44 (2008).
43. Polleux, F., Morrow, T. & Ghosh, A. Semaphorin 3A is a chemoattractant for cortical apical dendrites. *Nature* **404**, 567–573 (2000).
44. Yi, J. J., Barnes, A. P., Hand, R., Polleux, F. & Ehlers, M. D. TGF-beta signaling specifies axons during brain development. *Cell* **142**, 144–157 (2010).
45. D'Arcangelo, G. *et al.* A protein related to extracellular matrix proteins deleted in the mouse mutant reeler. *Nature* **374**, 719–723 (1995).
46. Pollen, A. A. *et al.* Molecular Identity of Human Outer Radial Glia during Cortical Development. *Cell* **163**, 55–67 (2015).
47. Fietz, S. A. *et al.* Transcriptomes of germinal zones of human and mouse fetal neocortex suggest a role of extracellular matrix in progenitor self-renewal. *PNAS* **109**, 11836–11841 (2012).
48. Long, K. R. *et al.* Extracellular Matrix Components HAPLN1, Lumican, and Collagen I Cause Hyaluronic Acid-Dependent Folding of the Developing Human Neocortex. *Neuron* **99**, 702-719.e6 (2018).
49. Götz, M., Bolz, J., Joester, A. & Faissner, A. Tenascin-C Synthesis and Influence on Axonal Growth During Rat Cortical Development. *European Journal of Neuroscience* **9**, 496–506 (1997).
50. Lochter, A. *et al.* J1/tenascin in substrate-bound and soluble form displays contrary effects on neurite outgrowth. *Journal of Cell Biology* **113**, 1159–1171 (1991).
51. Tucker, R. P. & Chiquet-Ehrismann, R. Tenascin-C: Its functions as an integrin ligand. *The International Journal of Biochemistry & Cell Biology* **65**, 165–168 (2015).
52. Rigato, F. *et al.* Tenascin-C Promotes Neurite Outgrowth of Embryonic Hippocampal Neurons through the Alternatively Spliced Fibronectin Type III BD Domains via Activation of the Cell Adhesion Molecule

F3/Contactin. *J. Neurosci.* **22**, 6596–6609 (2002).
53. Fawcett, J. W., Oohashi, T. & Pizzorusso, T. The roles of perineuronal nets and the perinodal extracellular matrix in neuronal function. *Nat. Rev. Neurosci.* **20**, 451–465 (2019).
54. Frischknecht, R. *et al.* Brain extracellular matrix affects AMPA receptor lateral mobility and short-term synaptic plasticity. *Nature Neuroscience* **12**, 897–904 (2009).
55. Kochlamazashvili, G. *et al.* The extracellular matrix molecule hyaluronic acid regulates hippocampal synaptic plasticity by modulating postsynaptic L-type Ca(2+) channels. *Neuron* **67**, 116–128 (2010).
56. Pizzorusso, T. *et al.* Reactivation of ocular dominance plasticity in the adult visual cortex. *Science* **298**, 1248–1251 (2002).
57. Miyata, S., Komatsu, Y., Yoshimura, Y., Taya, C. & Kitagawa, H. Persistent cortical plasticity by upregulation of chondroitin 6-sulfation. *Nat. Neurosci.* **15**, 414–422, S1-2 (2012).
58. Turk, B. E., Huang, L. L., Piro, E. T. & Cantley, L. C. Determination of protease cleavage site motifs using mixture-based oriented peptide libraries. *Nat Biotechnol* **19**, 661–667 (2001).
59. Zhou, X.-H. *et al.* Neurocan Is Dispensable for Brain Development. *Mol Cell Biol* **21**, 5970–5978 (2001).
60. Cichon, S. *et al.* Genome-wide association study identifies genetic variation in neurocan as a susceptibility factor for bipolar disorder. *Am J Hum Genet* **88**, 372–381 (2011).
61. Schultz, C. C. *et al.* Common variation in NCAN, a risk factor for bipolar disorder and schizophrenia, influences local cortical folding in schizophrenia. *Psychol Med* **44**, 811–820 (2014).
62. Raum, H. *et al.* A genome-wide supported psychiatric risk variant in NCAN influences brain function and cognitive performance in healthy subjects. *Hum Brain Mapp* **36**, 378–390 (2015).
63. Kathuria, A. *et al.* Transcriptome analysis and functional characterization of cerebral organoids in bipolar disorder. *Genome Med* **12**, 34 (2020).
64. Nakao, N., Hiraiwa, N., Yoshiki, A., Ike, F. & Kusakabe, M. Tenascin-C promotes healing of Habu-snake venom-induced glomerulonephritis: studies in knockout congenic mice and in culture. *Am J Pathol* **152**, 1237–1245 (1998).
65. Ohtsuka, M. *et al.* i-GONAD: a robust method for in situ germline genome engineering using CRISPR nucleases. *Genome Biol* **19**, 25 (2018).
66. Gurumurthy, C. B. *et al.* Creation of CRISPR-based germline-genome-engineered mice without ex vivo handling of zygotes by i-GONAD. *Nat Protoc* **14**, 2452–2482 (2019).
67. Sakurai, N. *et al.* Apical-to-basolateral transepithelial transport of cow's milk caseins by intestinal Caco-2 cell monolayers: MS-based quantitation of cellularly degraded α- and β-casein fragments. *J. Biochem.* **164**, 113–125 (2018).
68. Kongtawelert, P. & Ghosh, P. An enzyme-linked immunosorbent-inhibition assay for quantitation of hyaluronan (hyaluronic acid) in biological fluids. *Analytical Biochemistry* **178**, 367–372 (1989).
69. Kyu, M. T. *et al.* Predominant secretion of cellobiohydrolases and endo-β-1,4-glucanases in nutrient-limited medium by Aspergillus spp. isolated from subtropical field. *J. Biochem.* **168**, 243–256 (2020).
70. Evans, R. *et al.* Protein complex prediction with AlphaFold-Multimer. 2021.10.04.463034 Preprint at

https://doi.org/10.1101/2021.10.04.463034 (2022).

71. Mirdita, M. *et al.* ColabFold: making protein folding accessible to all. *Nat Methods* **19**, 679–682 (2022).
72. Katoh, K. & Standley, D. M. MAFFT multiple sequence alignment software version 7: improvements in performance and usability. *Mol Biol Evol* **30**, 772–780 (2013).
73. Robert, X. & Gouet, P. Deciphering key features in protein structures with the new ENDscript server. *Nucleic Acids Res* **42**, W320-324 (2014).
74. Laskowski, R. A., Jabłońska, J., Pravda, L., Vařeková, R. S. & Thornton, J. M. PDBsum: Structural summaries of PDB entries. *Protein Sci* **27**, 129–134 (2018).
75. Tina, K. G., Bhadra, R. & Srinivasan, N. PIC: Protein Interactions Calculator. *Nucleic Acids Res* **35**, W473-476 (2007).
76. Tabata, H. & Nakajima, K. Labeling embryonic mouse central nervous system cells by in utero electroporation. *Development, Growth & Differentiation* **50**, 507–511 (2008).
77. Mubuchi, A. *et al.* Isolation and structural characterization of bioactive glycosaminoglycans from the green-lipped mussel Perna canaliculus. *Biochemical and Biophysical Research Communications* **612**, 50–56 (2022).
78. Meijering, E. *et al.* Design and validation of a tool for neurite tracing and analysis in fluorescence microscopy images. *Cytometry A* **58**, 167–176 (2004).
79. Kanda, Y. Investigation of the freely available easy-to-use software 'EZR' for medical statistics. *Bone Marrow Transplant* **48**, 452–458 (2013).

1 **Key resources table**

REAGENT or RESOURCE	SOURCE	IDENTIFIER
Antibodies		
Anti-tenascin C Rat IgG2A (Clone # 578) Anti Tenascin	R&D	MAB2138
Anti-β-Tubulin (Tuj-1) Mouse IgG1(clone TUB 2.1)	Sigma	T4026
Anti-Neurocan Sheep IgG	R&D	AF5800
Anti-GFP Alexa Fluor 488 conjugate Rabbit IgG	Invitrogen	A21311
Anti-Nestin Mouse IgG	Millipore	2780475
Anti-Pax6 Rabbit IgG	Invitrogen	015-27293
Anti-EOMES (Tbr2) Rat IgG2A	Invitrogen	14-4875-82
Anti-GAPDH Mouse IgG1(Clone # 5A12)	Wako	016-25523
Anti-Chondroitine-4-Sulfate Mouse IgG1 (Clone # BE-123)	Millipore	2574085
Alexa Fluor 488 donkey anti-Mouse (H+L)	Wako	715-545-151
Alexa Fluor 594 goat anti-Rat IgG (H+L)	Thermo Fisher	A-11007
Alexa Fluor 647 goat anti-Rat IgG (H+L)	Thermo Fisher	A-21247
Alexa Fluor 647 donkey anti-Sheep IgG (H+L)	Thermo Fisher	A-21448
Mouse IgG HRP-conjugated Antibody	MBL	PM009-7
Sheep IgG HRP-conjugated Antibody	R&D	HAF016
Rat IgG HRP-conjugated Antibody	Cell Signaling Technology	7077S
Rabbit IgG HRP-conjugated Antibody	Cell Signaling Technology	7074S
Bacterial and virus strains		
Biological samples		
Chemicals, peptides, and recombinant proteins		
Alt-R S.p. Cas9 Nuclease V3	IDT	Catalog #1081058
Trypsin (Sequencing Grade)	Promega	V511C
HRP-conjugated streptavidin	Wako	190-17441
GFP-Trap-Agarose	Chromotek	gta-20
DAPI solution	DOJINDO	Lot.PF082 340-07971
N-2 Supplement	Thermo Fisher	17502-048
B-27 Supplement	Thermo Fisher	17504-044
Neurobasal Medium	Thermo Fisher	21103-049
Penicillin-Streptomycin	Thermo Fisher	15070-063
HBSS (X10)	Thermo Fisher	14185-052
HEPES (1M)	Thermo Fisher	15630-080

Papain	Worthington Biochemical Corporation	LK003178
Fast Green	Wako	061-00031
Protease Inhibitor Cocktail	Sigma	P8340-1ML
Streptavidin Magnetic Beads	Thermo Fisher	88817
Poly-L-Ornithine Solution	Wako	163-27421
Skim Milk Powder	Wako	190-12865
Immobilon Transfer Membrane PVDF	Millipore	IPVH00010
Immobilon Western Chemiluminescent	Millipore	WBKLS0500
Hyaluronidase from streptomyces hyalurolyticus	Sigma	H1136
Recombinant Human Tenascin C Protein	R&D	3358-TC
Recombinant Human Neurocan Protein	R&D	6508-NC-050
Chondroitinase ABC Protease Free	Seikagaku Corporation	100332
Sodium Hyaluronate (M2) (Mw:600,000~1,120,000)	PG Research	NaHA-M2
Biotinylated Sodium Hyaluronate (M1) (Mw:600,000~1,120,000)	PG Research	BHHA-M1
Carboxyfluorescein succinimidyl easter (CFSE)	DOJINDO	341-07401
ELISA 96 well plate	IWAKI	3801-096
BLOCK ACE Powder	KAC	UKB80
ELISA POD Substrate TMB Solution	Nacalai	05299-54
Hyaluronan Binding Protein (HABP)	Cosmo-bio	BC40
Hyaluronic Acid Sodium Salt	Wako	083-10341
Streptavidin, Alexa Fluor 488 conjugate	Thermo Fisher	S-11223
Biotinylated Hyaluronan Binding Protein	Hokudo	BC41
SuperScript III reverse transcriptase	Thermo Fisher	18080044
OCT Compound	Sakura Finetek	45833
Anion exchange chromatography resin	Tosoh	TOYOPEARL DEAE-650M
Heparin-agarose	Sigma	H6508
Ultrafiltration filter	Amicon	YM-10
α-cyano-4-hydroxyciccanic acid	Shimadzu	70990
Lipofectamine 3000 Reagent	Thermo Fisher	L3000008
Critical commercial assays		
BCA assay kit	Thermo Fisher	23227
RNeasy Mini Kit	Qiagen	74104

PowerUp SYBR Green Master Mix	Thermo Fisher	A25741
DIG RNA Labeling Kit (SP6/T7)	Roche	11175025910
NEBuilder HiFi DNA Assembly Master Mix	New England Biolabs	E2621
In-Fusion HD Cloning Kit	Takara	639648
KOD -Plus- Mutagenesis Kit	Toyobo	SMK-101
Deposited data		
Experimental models: Cell lines		
HEK293	Riken Cell Bank	RCB1637
Experimental models: Organisms/strains		
ICR mice	Japan SLC	RRID:MGI:5462094
C57BL/6N mice	Japan SLC	RRID:MGI:5295404
B6.Cg-Tnc<tm1Sia>/Rbrc	RIKEN Bioresource Center	RBRC00169
DKO mice for TNC and NCAN	This paper	N/A
Oligonucleotides		
ISH TNC probe f: CGGAATTCATCTTTGCAGAGAAAGGACAGC	This paper	N/A
ISH TNC probe r: GCTCTAGACTGTGTCCTTGTCATAGGTGGA	This paper	N/A
ISH NCAN probe f: GCGAATTCAGAATGCCTCTCTTGTTGGTG	This paper	N/A
ISH NCAN probe r: GCTCTAGACTACAATAGTGAGTTCGAGGCC	This paper	N/A
crRNA, Mm.Cas9.NCAN.1.AA: ACCUUAGUCCACUUGAUCCGGUUUUAGAGCUAUGCU	IDT	REF #101658344
Alt-R CRISPR-Cas9 tracrRNA	IDT	#1072533
qPCR for Ncan: forward, 5'-CCCTGCTTCTTTACCCTGCA-3'; reverse, 5'-CGTTGTCTTTGGCCACCAAG-3'	This paper	N/A
qPCR for Tnc: forward, 5'-ACCATGGGTACAGGCTGTTG-3'; reverse, 5'-CCTTTCCAGCCTGGTTCACA-3'	This paper	N/A

qPCR for Gapdh: forward, 5'-GACTTCAACAGCAACTCCCAC-3'; reverse, 5'-TCCACCACCCTGTTGCTGTA-3'	This paper	N/A
Recombinant DNA		
pCAG-GFP	Addgene	Plasmid #11150
pCAG-mGFP	Addgene	Plasmid #14757
pCAG-Full length NCAN-GFP	This paper	N/A
pCAG-N half NCAN-GFP	This paper	N/A
pCAG-C half NCAN-GFP	This paper	N/A
Software and algorithms		
MASCOT server	Matrix science	https://www.matrixscience.com/server.html
ImageJ	Schneider et al., 2012	https://imagej.nih.gov/ij/
Other		
Electroporator	NEPA GENE	NEPA21
5 mm-diameter tweezers-type disc electrodes	NEPA GENE	CUY650P5
2.5 mm x 4mm tweezers-type disc electrodes	NEPA GENE	CUY652P2.5X4
Vibratome	Leica	VT1200S
LuminoGraph	ATTO	WSE-6100H-ACP
Confocal laser scanning microscope	Nicon	AX
Confocal laser scanning microscope	Carl Zeiss	LSM 710 NLO
Fluorescence stereomicroscope	Leica	M165FC
Animal anesthetizer	Muromachi	MK-AT210
StepOne Real-Time PCR System	Thermo Fisher	4376374
Cryostat	Leica	CM3050 S
Direct nanoLC/MALDI fraction sytem	KYA technologies	DiNa-MaP
MALDI mass spectrometer	SCIEX	TOF/TOF 5800
LC-MS/MS System	SCIEX	QTRAP 5500
Fluorescence-activated cell sorter	Bay bioscience	JSAN

1